- Full paper contribution to ACTA GEOTECHNICA
- 8528 words
- 21 Figures and 4 Tables

A unified mechanical and retention model for saturated and unsaturated soil behaviour

Author 1

- Martí Lloret-Cabot, Ph.D
- Faculty of Engineering and Built Environment, University of Newcastle, Newcastle, Australia
- Formerly Universities of Strathclyde and Glasgow, Glasgow, UK

Author 2

- Simon J. Wheeler, Prof
- School of Engineering, University of Glasgow, Glasgow, UK

Author 3

- Marcelo Sánchez, A/Prof
- Department of Civil Engineering, Texas A & M University, Texas, USA
- Formerly University of Strathclyde, Glasgow, UK

Corresponding author
Martí Lloret Cabot
Marti.Lloretcabot@newcastle.edu.au
Faculty of Engineering and Built Environment
University of Newcastle
Callaghan, Building EA
NSW 2308
Australia
Tel. +61 2 4921 5660

ABSTRACT

The coupled mechanical and water retention elasto-plastic constitutive model of Wheeler, Sharma and Buisson (the Glasgow Coupled Model, GCM) predicts unique unsaturated isotropic normal compression and unsaturated critical state planar surfaces for specific volume and degree of saturation when soil states are at the intersection of Mechanical (*M*) and Wetting Retention (*WR*) yield surfaces. Experimental results from tests performed by Sivakumar on unsaturated samples of compacted speswhite kaolin confirm the existence and form of these unique surfaces. The GCM provides consistent representation of transitions between saturated and unsaturated conditions, including the influence of retention hysteresis and the effect of plastic volumetric strains on retention behaviour, and it gives unique expressions to predict saturation and de-saturation conditions (air-exclusion and air-entry points respectively). Mechanical behaviour is modelled consistently across these transitions, including appropriate variation of mechanical yield stress under both saturated and unsaturated conditions. The expressions defining the unsaturated isotropic normal compression planar surfaces for specific volume and degree of saturation are central to the development of a relatively straightforward methodology for determining values of all GCM parameters (soil constants and initial state) from a limited number of laboratory tests. This methodology is demonstrated by application to the experimental data of Sivakumar. Comparison of model simulations with experimental results for the full set of Sivakumar's isotropic loading stages demonstrates that the model is able to predict accurately the variation of both specific volume and degree of saturation during isotropic stress paths under saturated and unsaturated conditions.

Keywords: unsaturated soils, saturated soils, constitutive relations, mechanical behaviour, water retention, suction, saturation, de-saturation, retention hysteresis

INTRODUCTION

Wheeler et al. [51] developed a coupled elasto-plastic constitutive model for unsaturated soils, which represents both mechanical behaviour and water retention behaviour, including the coupling between them. The model, originally presented solely for isotropic stress states, has subsequently been extended to general stress states (e.g. Lloret-Cabot et al. [24]) and is referred to hereafter as the Glasgow Coupled Model (GCM). In the model, a single yield surface represents mechanical behaviour, with plastic volumetric strains $d\varepsilon_v^p$ and plastic deviatoric strains $d\varepsilon_q^p$ occurring during yielding on this surface. Two other yield surfaces represent water retention behaviour, with plastic changes of degree of saturation dS_r^p occurring during yielding on either of these surfaces. Coupled movements of the three yield surfaces represent the influence of plastic changes of degree of saturation on mechanical behaviour and the influence of plastic volumetric strains on water retention behaviour.

In this paper it is shown that the GCM predicts unique expressions for specific volume v and degree of saturation S_r for stress states involving simultaneous mechanical yielding (occurrence of plastic compression) and wetting retention yielding (occurrence of plastic increases of S_r). These expressions for v and S_r facilitate significantly the use and interpretation of the model, including determination of model parameter values from experimental test data.

A major challenge of constitutive models for unsaturated soils is the correct representation of transitions between unsaturated and saturated conditions. The challenge of properly modelling such transitions is intimately linked to consistent consideration of retention hysteresis and to the choice of stress state variables, with particular difficulties for conventional models expressed in terms of net stresses (excess of total stress over pore air pressure) and suction (difference between pore air pressure and pore water pressure), because de-saturation during drying will not occur at zero suction and subsequent re-saturation on wetting will occur at a different value of suction. This paper shows how the GCM is able to provide consistent representation of transitions between unsaturated and saturated states, through the use of non-conventional stress state variables and proper consideration of retention hysteresis. The model gives unique expressions to predict saturation and de-saturation conditions,

which account for both retention hysteresis and the influence of plastic volumetric strains on retention behaviour, and it provides consistent modelling of mechanical behaviour across these transitions.

THE GLASGOW COUPLED MODEL (GCM)

The stress variables used in the GCM are "Bishops's stress" tensor σ_{ij}^* (sometimes also called "average soil skeleton stress", Jommi [19]) and "modified suction" s^*. The stress tensor σ_{ij}^* is similar to the effective stress expression proposed by Bishop in 1959 [4] but with his weighting factor χ replaced by the degree of saturation (as suggested in Schrefler [36]). For the restricted range of stress states that apply in the triaxial test, it is sufficient to consider only mean Bishop's stress p^*, deviator stress q and modified suction s^*, defined as follows:

$$p^* = p - S_r u_w - (1 - S_r) u_a = \bar{p} + S_r s \tag{1}$$

$$q = \sigma_1 - \sigma_3 \tag{2}$$

$$s^* = n(u_a - u_w) = ns \tag{3}$$

where p is mean total stress, u_w is pore water pressure, u_a is pore air pressure, σ_1 and σ_3 are, respectively, major and minor principal total stresses and n is porosity. $\bar{p}$ and s are mean net stress and matric suction respectively, where $\bar{p}$, q and s are the stress variables used in many more conventional mechanical constitutive models for unsaturated soils, such as the Barcelona Basic Model (BBM) of Alonso et al. [1]. The stress variables p^*, q and s^* are work-conjugate with volumetric strain increment $d\varepsilon_v$, deviatoric strain increment $d\varepsilon_q$ and decrement of degree of saturation $-dS_r$ respectively (Houlsby [18]).

Elastic components of $d\varepsilon_v$, $d\varepsilon_q$ and $-dS_r$ are given by:

$$d\varepsilon_v^e = \frac{\kappa dp^*}{vp^*} \tag{4}$$

$$d\varepsilon_q^e = \frac{dq}{3G} \tag{5}$$

$$-dS_r^e = \frac{\kappa_s ds^*}{s^*} \tag{6}$$

where κ is the elastic swelling index, giving the gradient of elastic swelling lines in the $v{:}\ln p^*$ plane (mechanical behaviour), G is the elastic shear modulus (mechanical behaviour) and κ_s is the gradient of elastic scanning curves in the $S_r{:}\ln s^*$ plane (water retention behaviour).

The model includes three yield surfaces in $p^*{:}q{:}s^*$ space: a Mechanical (*M*) yield surface to represent mechanical behaviour (originally referred to as the Loading Collapse (*LC*) yield surface in Wheeler et al. [51]) and Wetting Retention (*WR*) and Drying Retention (*DR*) yield surfaces to represent water retention behaviour (originally referred to as, respectively, the Suction Decrease (*SD*) and Suction Increase (*SI*) yield surfaces). Plastic volumetric strains and plastic deviatoric strains occur during yielding on the *M* surface, whereas plastic changes of degree of saturation occur during yielding on *WR* or *DR* surfaces. The re-naming of the yield surfaces from the original terminology used in [51] is to make explicit the fact that the *M* surface is the only one of the three describing mechanical yielding (and this can occur during loading, wetting or drying, see Lloret-Cabot et al. [25]), whereas the other two describe retention behaviour. This contrasts with the BBM, where both *LC* and *SI* yield surfaces represent mechanical behaviour (Alonso et al. [1]).

The equations of *M*, *WR* and *DR* surfaces are given respectively by:

$$q^2 - \mathrm{M}^2 p^* \left(p_0^* - p^* \right) = 0 \tag{7}$$

$$s_1^* - s^* = 0 \tag{8}$$

$$s^* - s_2^* = 0 \tag{9}$$

where M is a soil constant and p_0^*, s_1^* and s_2^* are hardening parameters defining the current positions of the *M*, *WR* and *DR* yield surfaces respectively (Figure 1).

Equation 7 indicates that constant s^* cross-sections of the mechanical yield surface are elliptical in shape (of aspect ratio M) and the size p_0^* of these cross-sections does not vary with s^*. Equations 8 and 9 indicate that the *WR* and *DR* surfaces form vertical walls in p^*:q:s^* space (Figure 1).

Associated flow rules are assumed on all three yield surfaces. This means that yielding on the M surface alone corresponds to:

$$\frac{d\varepsilon_q^p}{d\varepsilon_v^p} = \frac{2\eta^*}{\mathrm{M}^2 - \left(\eta^*\right)^2} \qquad \text{and} \qquad dS_r^p = 0 \tag{10}$$

where $\eta^* = q/p^*$. Similarly, yielding on the *WR* surface alone corresponds to:

$$d\varepsilon_q^p = d\varepsilon_v^p = 0 \qquad \text{and} \qquad dS_r^p > 0 \tag{11}$$

and yielding on the *DR* surface alone corresponds to:

$$d\varepsilon_q^p = d\varepsilon_v^p = 0 \qquad \text{and} \qquad dS_r^p < 0 \tag{12}$$

The hardening law giving movements of the M yield surface includes a direct component of movement caused by plastic volumetric strain (due to yielding on the M surface) but also a second (coupled) component of movement caused by any plastic changes of S_r due to yielding on *WR* or *DR* surfaces:

$$\frac{dp_0^*}{p_0^*} = \frac{v d\varepsilon_v^p}{\lambda - \kappa} - k_1 \frac{dS_r^p}{\lambda_s - \kappa_s} \tag{13}$$

where λ and κ are the gradients of normal compression lines and swelling lines respectively in the v: $\ln p^*$ plane for isotropic loading and unloading tests involving no plastic changes of S_r (such as saturated tests), λ_s and κ_s are the gradients of main wetting/drying curves and scanning curves respectively in the S_r: $\ln s^*$ plane (see Figure 2a) for retention tests involving no plastic volumetric strains, and k_1 is a coupling parameter.

Similarly, the hardening law giving movements of the *WR* or *DR* yield surfaces includes a direct component of movement caused by plastic change of S_r (due to yielding on

the *WR* or *DR* surface) and a second (coupled) component of movement caused by any plastic volumetric strains due to yielding on the *M* surface:

$$\frac{ds_1^*}{s_1^*} = \frac{ds_2^*}{s_2^*} = -\frac{dS_r^p}{\lambda_s - \kappa_s} + k_2 \frac{v d\varepsilon_v^p}{\lambda - \kappa} \tag{14}$$

where k_2 is a second coupling parameter. Equation 14 ensures that the movements of the *DR* and *WR* yield surfaces are such that the ratio of s_2^* to s_1^* (the spacing of the *DR* and *WR* surfaces when plotted in terms of $\ln s^*$) remains constant:

$$\frac{s_2^*}{s_1^*} = R \tag{15}$$

where R is a soil constant.

The special cases of the hardening laws during yielding on only a single yield surface (*M*, *WR* or *DR*) are given by inserting the relevant condition from Equation 10, 11 or 12 ($dS_r^p = 0$ or $d\varepsilon_v^p = 0$) into Equations 13 and 14.

When the soil reaches a saturated condition ($S_r = 1$), further elastic increases of S_r are prevented (Equation 6 no longer applies for decreases of s^*) and further plastic increases of S_r are prevented ($d\varepsilon_q^p = d\varepsilon_v^p = dS_r^p = 0$ replaces Equation 11 for states on the *WR* yield surface alone). In addition, the consistency condition on the *WR* yield surface is removed, so that the stress state can pass beyond the *WR* surface. This is illustrated in Figure 2, with Figure 2a showing water retention behaviour (for conditions of no plastic volumetric straining), including a saturated point X, and Figure 2b showing the corresponding positions of the yield curves when the stresses are at point X. While the soil is saturated, the *M* yield surface is still operative, and Equation 13 (with $dS_r^p = 0$) recovers the conventional Modified Cam Clay hardening law (Roscoe and Burland [35]). Also, while the soil is saturated, Equation 14 (with $dS_r^p = 0$) is still used to determine coupled movements of the *WR* and *DR* surfaces caused by plastic volumetric strain. This represents changes of air entry value caused by plastic volumetric strain.

The model predicts the occurrence of critical states that correspond to the apex of the elliptical cross-sections of the M yield surface and hence it predicts a unique critical state line in the $q{:}p^*$ plane:

$$q = \mathrm{M}p^* \tag{16}$$

The assumption of a unique critical state line in the $q{:}p^*$ plane has been demonstrated for a range of compacted non-expansive fine grained soils (e.g. Gallipoli et al. [16], Lloret-Cabot et al. [24]).

DERIVATION AND VALIDATION OF EXPRESSIONS FOR v AND S_r

Isotropic normal compression states

Due to the coupled movements of the yield surfaces, there is a very wide variety of isotropic stress paths that will ultimately arrive at the intersection between M and WR surfaces (Point A in Figure 3). For example, if yield occurs first on the M surface, this will cause a coupled movement of the WR surface, which after a while will typically bring the WR surface to the stress point. Similarly, if yield occurs first on the WR surface, this will cause a coupled inward movement of the M surface, which after a while will typically bring the M surface in to the stress point. More generally, any stress paths where plastic volumetric strains and plastic increases of S_r occur simultaneously correspond to this intersection of M and WR surfaces. Inspection of the literature indicates that this behaviour applies to the majority of published experimental data for normal compression states. This is because the occurrence of plastic compression typically observed during isotropic (or one dimensional) loadings at constant suction reduces porosity and, when such reduction is sufficiently large, irreversible increases of S_r are also observed, even though suction remains constant during the test (e.g. [8, 10, 13, 14, 22, 28-30, 32-34, 37, 41, 42, 44, 45, 47, 49, 51]). This type of response is also very often observed in available experimental data showing collapse compression behaviour on wetting (e.g. [13, 14, 22, 28-30, 32-34, 37, 41, 42, 44, 51]). In this case, the plastic increases of S_r caused when decreasing suction tend to reduce the stability of the soil skeleton [51] and this loss of stability may potentially result in volumetric

compression [25]. From a theoretical point of view, a proper representation of this coupling between variations of volumetric strains (mechanical behaviour) and variations of degree of saturation or suction (retention behaviour) during loading and wetting paths has been the focus of a large number of constitutive relationships proposed in the literature (e.g. [1, 3, 9, 12, 13-15, 20, 21, 23-27, 31, 34, 39, 40, 46, 48, 49, 51-53]), because they potentially play a critical role in the geotechnical response of boundary value problems involving unsaturated soils (e.g. [2, 5-7, 11, 17, 22, 38, 43]).

What can now be shown is that the model predicts unique expressions for v and S_r for these isotropic normal compression states at the intersection of *M* and *WR* surfaces.

Combining Equations 13 and 14 gives the following expressions for $d\varepsilon_v^p$ and $-dS_r^P$ in terms of the movements of the *M* and *WR* yield surfaces:

$$d\varepsilon_v^p = \frac{(\lambda-\kappa)}{v(1-k_1k_2)}\left(\frac{dp_0^*}{p_0^*} - k_1\frac{ds_1^*}{s_1^*}\right) \tag{17}$$

$$-dS_r^p = \frac{(\lambda_s-\kappa_s)}{(1-k_1k_2)}\left(\frac{ds_1^*}{s_1^*} - k_2\frac{dp_0^*}{p_0^*}\right) \tag{18}$$

Equations 4 and 17, for the elastic and plastic components of volumetric strain, can be combined, in order to give the total volumetric strain increment and hence the total increment of v :

$$dv = -\frac{\kappa dp^*}{p^*} - \frac{(\lambda-\kappa)}{(1-k_1k_2)}\left(\frac{dp_0^*}{p_0^*} - k_1\frac{ds_1^*}{s_1^*}\right) \tag{19}$$

For an isotropic stress state at the intersection between *M* and *WR* surfaces ($p_0^* = p^*$ and $s_1^* = s^*$) and an isotropic stress increment remaining at this intersection ($dp_0^* = dp^*$ and $ds_1^* = ds^*$), Equation 19 simplifies to:

$$dv = -\lambda^*\frac{dp^*}{p^*} + k_1^*\frac{ds^*}{s^*} \tag{20}$$

where:

$$\lambda^* = \frac{\lambda - k_1 k_2 \kappa}{1 - k_1 k_2} \tag{21}$$

$$k_1^* = k_1 \frac{(\lambda - \kappa)}{(1 - k_1 k_2)} \tag{22}$$

Integration of Equation 20 indicates that the model predicts that values of v for isotropic normal compression states at the intersection of *M* and *WR* yield surfaces are given by the following unique expression:

$$v = \mathrm{N}^* - \lambda^* \ln p^* + k_1^* \ln s^* \tag{23}$$

where λ^* and k_1^* are soil constants given by Equations 21 and 22, and N^* is an additional soil constant. Equation 23 represents a planar surface in $v : \ln p^* : \ln s^*$ space, as shown in Figure 4.

A similar procedure for the variation of S_r shows that the model predicts that values of S_r for isotropic normal compression states at the intersection of *M* and *WR* yield surfaces are given by:

$$S_r = \Omega^* - \lambda_s^* \ln s^* + k_2^* \ln p^* \tag{24}$$

where λ_s^* and k_2^* are soil constants given by:

$$\lambda_s^* = \frac{\lambda_s - k_1 k_2 \kappa_s}{1 - k_1 k_2} \tag{25}$$

$$k_2^* = k_2 \frac{(\lambda_s - \kappa_s)}{(1 - k_1 k_2)} \tag{26}$$

and Ω^* is an additional soil constant. Equation 24 represents a planar surface in S_r: $\ln p^* : \ln s^*$ space, as shown in Figure 5.

General states

Expressions for v and S_r for any general stress state (see Point B in Figure 3) can now be derived by considering an elastic stress path from A (coordinates p_0^*, 0, s_1^*) to B (coordinates p^*, q, s^*):

$$v = \mathrm{N}^* - \lambda^* \ln p_0^* + k_1^* \ln s_1^* + \kappa \ln\left(\frac{p_0^*}{p^*}\right) \tag{27}$$

$$S_r = \Omega^* - \lambda_s^* \ln s_1^* + k_2^* \ln p_0^* - \kappa_s \ln\left(\frac{s^*}{s_1^*}\right) \tag{28}$$

Equations 27 and 28 provide general expressions for v and S_r for any stress state (p^*, q, s^*) when the current locations of the *M* and *WR* yield surfaces are given by p_0^* and s_1^* respectively.

For the particular case of isotropic stress states at the intersection between *M* and *DR* surfaces (Point C in Figure 3), $p^* = p_0^*$, $s^* = Rs_1^*$ and Equations 27 and 28 give:

$$v = \mathrm{N}^* - k_1^* \ln R - \lambda^* \ln p^* + k_1^* \ln s^* \tag{29}$$

$$S_r = \Omega^* + \left(\lambda_s^* - \kappa_s\right)\ln R - \lambda_s^* \ln s^* + k_2^* \ln p^* \tag{30}$$

Critical states

The model predicts that critical states can correspond to any points at the apex of the *M* yield surface, such as Points D, E and F in Figure 3. In practice, however, it will normally happen that critical states correspond to the intersection with the *WR* yield surface (i.e. Point D in Figure 3), because yielding on the *M* surface will cause coupled movement of the *WR* surface that will be sufficient to bring the *WR* surface to the stress point prior to arrival at a critical state.

Expressions for v and S_r for critical states corresponding to the intersection of *M* and *WR* yield surfaces (Point D in Figure 3) can be derived from the general expressions of Equations 27 and 28 by inserting $p_0^* = 2p^*$ (based on the elliptical shape of constant s^* cross-sections of the *M* surface) and $s_1^* = s^*$. This gives:

$$v = \Gamma^* - \lambda^* \ln p^* + k_1^* \ln s^* \quad (31)$$

$$S_r = \Psi^* - \lambda_s^* \ln s^* + k_2^* \ln p^* \quad (32)$$

where Γ^* and Ψ^* are given by:

$$\Gamma^* = \mathrm{N}^* - \left(\lambda^* - \kappa\right)\ln 2 \quad (33)$$

$$\Psi^* = \Omega^* + k_2^* \ln 2 \quad (34)$$

Equations 31 and 32 define two unique critical state planar surfaces, in $v{:}\ln p^*{:}\ln s^*$ and $S_r{:}\ln p^*{:}\ln s^*$ spaces respectively. Comparison with Equations 23 and 24 indicates that these critical state surfaces for v and S_r are predicted to be parallel to the corresponding normal compression surfaces.

Experimental validation for isotropic normal compression states

Experimental data from the tests of Sivakumar [41] on compacted speswhite kaolin are used to investigate the validity of the model predictions of unique planar surfaces for v and S_r for both isotropic normal compressions states and critical states.

Experimental results are taken from 15 constant suction isotropic loading tests performed by Sivakumar [41] on unsaturated samples at three different values of suction s (100, 200 and 300 kPa). In each unsaturated test, the isotropic loading was preceded by an initial equalisation stage, as the sample was wetted from a substantially higher as-compacted value of suction. In all cases, plastic increases of degree of saturation occurred during the equalisation stage and plastic volumetric strains and increases of S_r occurred during the isotropic loading stage, consistent with soil states at the intersection of *M* and *WR* yield surfaces.

Figures 4 and 5 show experimental values of v and S_r from each isotropic loading unsaturated test that corresponded to soil states at the intersection of *M* and *WR* yield surfaces plotted in $v{:}\ln p^*{:}\ln s^*$ and $S_r{:}\ln p^*{:}\ln s^*$ spaces respectively, together with the corresponding best-fit planar surfaces obtained by least-squares multiple regression.

The gradients and intercepts of these best-fit surfaces gave values for λ^*, k_1^*, λ_s^*, k_2^*, N^* and Ω^* (see Equations 23 and 24), which are listed in Table 1.

A clearer view of the quality of fit shown in the three-dimensional representation presented in Figure 4 is provided by re-plotting the experimental data and best-fit surface for v in a pair of orthogonal two-dimensional views in Figure 6, using a form of plotting where the best-fit surface is reduced to a single straight line in each of the two views. Figure 7 provides an equivalent representation for S_r. Inspection of Figures 6 and 7 indicates that the two planar surfaces (for v and S_r) provide excellent fits to the experimental data.

Experimental validation for critical states

Each of the experimental tests of Sivakumar [41] involved shearing to failure after the isotropic loading stage. Figures 8 and 9 show the experimental critical state values of v and S_r plotted in $v{:}\ln p^*{:}\ln s^*$ and $S_r{:}\ln p^*{:}\ln s^*$ spaces respectively, together with the corresponding best-fit planar surfaces obtained by least-squares multiple regression. The gradients and intercepts of these best-fit surfaces gave values for λ^*, k_1^*, λ_s^*, k_2^*, Γ^* and Ψ^* (see Equations 31 and 32), which are listed in Table 2.

Figures 10 and 11 show pairs of orthogonal two-dimensional views of the critical state results, presented in suitable form so that, in each view, the fitted planar surface is reduced to a single straight line. Inspection of Figures 10 and 11 shows that the experimental critical state results for v and S_r show a degree of scatter, but approximate to planar surfaces in $v{:}\ln p^*{:}\ln s^*$ and $S_r{:}\ln p^*{:}\ln s^*$ spaces respectively.

Tables 1 and 2 include the two sets of experimentally determined values of λ^*, k_1^*, λ_s^*, and k_2^* from isotropic normal compression states and critical states respectively. Inspection of these tables show that the two different sets of values of λ^* and k_1^* (giving the gradients of the planar surfaces for v) show good consistency. The values of λ_s^* and k_2^* (giving the gradients of the planar surfaces for S_r) show larger differences between the two sets.

Figure 12 shows a pair of orthogonal two-dimensional representations of the isotropic normal compression and critical state data for v. The continuous lines in Figure 12 represent the best-fit planar surface to the experimental isotropic normal compression data, whereas the dashed lines represent the form of the critical state surface for v predicted by the model (Equations 31 and 33), if values of N^*, λ^*, and k_1^* determined from the isotropic normal compression planar surface are employed. Inspection of the experimental critical state values of v shows that the two planar surfaces for v are approximately parallel, as predicted by the model, but that the vertical spacing between the critical state and isotropic normal compression surfaces for v is significantly over-predicted by the model. The over-prediction of the spacing between the two planar surfaces for v is a consequence of the assumed elliptical shape of constant s^* cross-sections of the M yield surface [24] which could be adjusted following similar developments with constitutive models for saturated soils. For example, Wheeler et al. [50] show that incorporation of evolving plastic anisotropy in an elasto-plastic constitutive model for saturated clays (by means of an inclined yield curve with evolving inclination) reduces the predicted spacing between critical state line and isotropic normal compression line in the v: $\ln p'$ plane.

Figure 13 shows an equivalent pair of orthogonal two-dimensional representations of the isotropic normal compression and critical state data for S_r. Values of Ω^*, λ_s^* and k_2^* determined from the isotropic normal compression planar surface (the solid lines) are employed here to plot the dashed lines, which represent the form of the critical state surface predicted by the model (Equations 32 and 34). Inspection of Figure 13 shows that the vertical spacing between the critical state and isotropic normal compression surfaces for S_r predicted by the model provides a reasonable match to the experimental data, although there is significant scatter.

MODELLING TRANSITIONS BETWEEN UNSATURATED AND SATURATED BEHAVIOUR

The GCM covers both unsaturated states ($S_r < 1$) and saturated states ($S_r = 1$). For saturated states, the GCM recovers naturally the incremental mechanical constitutive

relationships of the MCC model for saturated soils. This is a direct consequence of using Bishop's stress σ_{ij}^{*} as a stress variable of the model because, by definition, σ_{ij}^{*} becomes the saturated effective stress σ'_{ij} when S_r = 1, which does not occur for the conventional net stress variable $\bar{\sigma}_{ij}$ unless $s = 0$ (see Equation 1).

For isotropic stress states on the *M* yield surface, as S_r reaches 1 the GCM response for *v* should converge to the conventional saturated Normal Compression Line, NCL:

$$v = \mathrm{N} - \lambda \ln p' \qquad (35)$$

where λ and N are, respectively, the gradient and intercept of the saturated NCL in the $v{:}\ln p'$ plane and p' is the saturated mean effective stress. Manipulation of Equations 23 and 24, defining the unsaturated isotropic normal compression planar surfaces for v and S_r, shows that for the unsaturated normal compression surface for v (given by Equation 23) to converge to the saturated NCL (Equation 35) at S_r = 1 (as given by Equation 24), it is necessary that κ_s = 0. This restriction on the value of κ_s is a consequence of a small inconsistency in the GCM model highlighted by Raveendiraraj [32], which is associated with any occurrence of plastic volumetric strains while the soil is fully saturated (or fully dry), as illustrated in Figure 14.

Figure 14 shows a wetting stress path ABC, followed by a loading-unloading cycle CDE (not seen in the figure) while the soil is saturated and then a drying path EFG. The loading-unloading cycle is such that during CDE plastic volumetric strain occurs, due to yielding on the *M* surface, whereas for simplicity it is assumed that no plastic volumetric strains occur during either AB or FG, while the soil is unsaturated. As a consequence of the plastic volumetric strain occurring while the soil is saturated, coupled movements of the *WR* and *DR* yield surfaces occur and this means that the water retention curves translate from the positions shown by the fine continuous lines in Figure 14 to those shown by the fine dashed lines. As a consequence, whereas the soil reaches a saturated state at a value of modified suction s_{B}^{*} during wetting, de-saturation occurs at a higher value of modified suction s_{F}^{*} during subsequent drying. This means that elastic increases of S_r occur over the range of modified suction s_{F}^{*} to s_{B}^{*} during the wetting path (plastic changes of S_r also occur) but that elastic decreases of S_r do not occur between s_{B}^{*} and s_{F}^{*} during the drying path. This means

that elastic changes of S_r have not been reversible over the range of modified suction s_B^* to s_F^*, which contravenes a basic tenet of elastic behaviour.

The predicted irreversibility of elastic changes of S_r introduces inconsistency into the model, by incorporating permanent distinction between the effects of past plastic volumetric strains occurring at saturated states and those occurring at unsaturated states (Raveendiraraj [32]). A simple way to overcome this problem is by assuming $\kappa_s = 0$, but inevitably this may result in slight deterioration in the representation of water retention behaviour. This sacrifice is, however, surprisingly small, because experimental values of κ_s determined from tests on compacted fine-grained soils are typically very small (e.g. [24-26]). It is therefore recommended that $\kappa_s = 0$ is assumed when the GCM is used in situations where transitions between unsaturated and saturated conditions occur (reducing by one the number of soil constants within the model).

With $\kappa_s = 0$, Figure 15 shows a three-dimensional view (in $v : \ln p^* : \ln s^*$ space) of both the unsaturated isotropic normal compression planar surface for v corresponding to the intersection of *M* and *WR* yield surfaces and the saturated isotropic normal compression line (which forms a planar surface parallel to the $\ln s^*$ axis in this three-dimensional space). The intersection of the two surfaces defines a "saturation line" corresponding to the transition from unsaturated to saturated conditions. Figure 16 shows the equivalent surfaces for S_r (in $S_r : \ln p^* : \ln s^*$ space), with the intersection between unsaturated and saturated surfaces corresponding to the same saturation line as in Figure 15. Also shown in Figures 15 and 16 is a typical stress path ASB involving transition from unsaturated to saturated conditions at point S.

Derivation of expressions for saturation and de-saturation lines

Adopting $\kappa_s = 0$, Equations 21 and 22 remain unchanged, and Equations 25 and 26 become:

$$\lambda_s^* = \frac{\lambda_s}{1 - k_1 k_2} \qquad (36)$$

$$k_2^* = k_2 \frac{\lambda_s}{\left(1 - k_1 k_2\right)} \tag{37}$$

Putting S_r = 1 in Equation 24, which defines the unsaturated normal compression planar surface for S_r , with λ_s^* and k_2^* given by Equations 36 and 37, produces an expression for the saturation line shown in Figures 15 and 16:

$$\ln s^* = \frac{\Omega^* - 1}{\lambda_s^*} + k_2 \ln p^* \tag{38}$$

Inserting the expression for the saturation line of Equation 38 in the expression for the unsaturated normal compression planar surface for *v* (Equation 23), gives an expression for the saturated NCL:

$$v = \mathrm{N}^* - \frac{k_1\left(\lambda - \kappa\right)}{\lambda_s}\left(1 - \Omega^*\right) - \lambda \ln p^* \tag{39}$$

Comparing Equation 39 with the standard expression for the saturated NCL (Equation 35), and remembering $p^* = p'$ when $S_r = 1$, shows that the intercepts Ω^*, N^* and N are related:

$$\Omega^* = 1 - \frac{\left(\mathrm{N}^* - \mathrm{N}\right)\lambda_s}{k_1\left(\lambda - \kappa\right)} \tag{40}$$

The saturation line defined by Equation 38 represents the combinations of s^* and p^* at which transitions from unsaturated to saturated conditions will occur if the stress state is isotropic and at the intersection between *M* and *WR* yield surfaces. With $\kappa_s = 0$, transitions from unsaturated to saturated conditions can only occur whilst on the *WR* yield surface, but it is not necessary for the stress state to be on the *M* yield surface or for the stress state to be isotropic at the point of transition from unsaturated to saturated conditions. Given that changes of p^* or q do not produce elastic changes of S_r , it is straightforward to use Equation 38 to derive a generalised expression for transition from unsaturated to saturated conditions, applicable to any isotropic or anisotropic stress states, including those not on the *M* yield surface, by considering an elastic stress path

along the *WR* yield surface from the intersection with the *M* yield surface at $q = 0$. This generalised expression for transition from unsaturated to saturated conditions under any stress state takes the form:

$$\ln s^* = \frac{\Omega^* - 1}{\lambda_s^*} + k_2 \ln p_0^* \tag{41}$$

This can be re-written as:

$$s^* = \exp\left(\frac{\Omega^* - 1}{\lambda_s^*}\right)\left(p_0^*\right)^{k_2} \tag{42}$$

The general expression for the saturation line, corresponding to transition from unsaturated to saturated conditions (sometimes known as the air-exclusion point), defined by Equation 41 or Equation 42, is illustrated in Figure 17 (in both a log-log plot and a linear plot). Note that Equations 41 and 42 and Figure 17 show that the saturation value of s^* is uniquely dependent on the position of the *M* yield surface (i.e. the value of p_0^*).

Transitions in the reverse direction, from saturated to unsaturated conditions, must occur on the *DR* yield surface if $\kappa_s = 0$, but it is not necessary for the stress state at the point of de-saturation to be on the *M* surface. This transition from saturated to unsaturated conditions occurs on a "de-saturation line" defined by:

$$s^* = R \exp\left(\frac{\Omega^* - 1}{\lambda_s^*}\right)\left(p_0^*\right)^{k_2} \tag{43}$$

where R is the soil constant defining the fixed ratio of s_2^* to s_1^* (see Equation 15).

Figure 17 shows the form of the de-saturation line defined by Equation 43, corresponding to transition from saturated to unsaturated conditions (sometimes known as the air-entry point).

Figure 17 illustrates that the GCM includes the influences of both retention hysteresis and plastic volumetric straining on transitions between saturated and unsaturated

conditions. The difference between the saturation and de-saturation values of s^* (at the same value of p_0^*) shows the influence of retention hysteresis, whereas the variation of both saturation and de-saturation values of s^* with p_0^* shows the influence of plastic volumetric strains on air-exclusion and air-entry points.

Mechanical yielding under saturated and unsaturated conditions

Figure 18 illustrates how the GCM provides consistent modelling of mechanical yielding under both saturated and unsaturated conditions. The figure shows a wetting-drying cycle ABCDEF involving transitions between unsaturated and saturated conditions during both wetting and drying (at points B and E respectively). The stress path starts on the *WR* yield surface at A but remains inside the *M* yield surface throughout. The stress path shown in Figure 18 in both the $s^* : p^*$ plane (Figure 18a) and the conventional $s : \bar{p}$ plane (Figure 18b) happens to represent a wetting-drying cycle performed at constant $\bar{p}$, but the discussion presented in this section would apply equally well to any general wetting-drying path remaining inside the *M* yield surface.

Also shown in Figure 18a is the variation of mechanical yield stress p_0^* predicted by the GCM during the wetting-drying cycle, representing the coupled movement of the *M* yield surface. The value of p_0^* reduces during the initial unsaturated section AB of the wetting path, due to the coupled inward movement of the *M* surface caused by the plastic increases of S_r during yielding on the *WR* surface (see Equation 13). However, during the final saturated section BC of the wetting path, the value of p_0^* remains constant, as there are no longer any plastic increases of S_r to produce further coupled movement of the *M* surface. During drying path CDEF the stress path passes back inside the *WR* surface at point D, but de-saturation only occurs when the stress path reaches the *DR* surface at E. The value of p_0^* therefore remains constant during the initial saturated section CDE of the drying path and then increases during the final unsaturated section EF (see Equation 13).

Figure 18b shows the variation of mechanical yield stress predicted by the GCM during the wetting-drying cycle ABCDEF re-plotted in the conventional $s : \bar{p}$ plane. The

variation of mechanical yield stress during the unsaturated section AB of the wetting path is equivalent to the *LC* yield curve in conventional models such as the BBM. From B to C, however, with the soil in a saturated condition, the variation of mechanical yield stress for the GCM plots as a 45° line in the $s:\bar{p}$ plane, consistent with yield at a constant value of saturated mean effective stress ($p' = p - u_w = \bar{p} + s$). During the drying path CDEF the variation of mechanical yield stress follows a 45° line until the soil de-saturates at E, and then from E to F it forms a curve again. The qualitative form of variation of mechanical yield stress shown in Figure 18b is exactly what would be expected for a soil under unsaturated and saturated conditions, where saturation occurs at a non-zero air-exclusion value of suction (point B) and de-saturation occurs at a non-zero air-entry value of suction (point E) that is higher than the air-exclusion value because of hysteresis in the retention behaviour. This variation of mechanical yield stress emerges naturally from the GCM, whereas it would be very difficult to achieve in any mechanical model expressed in terms of net stresses and suction.

DETERMINATION OF MODEL PARAMETER VALUES

With $\kappa_s = 0$, the GCM involves 10 soil constants: λ, κ, N, M, G, N^*, k_1, k_2, λ_s and R. The first 5 constants are the Modified Cam Clay parameters, required for modelling of mechanical behaviour under saturated conditions, whereas the other 5 constants are required to extend the modelling to include mechanical behaviour under unsaturated conditions, water retention behaviour and the coupling between them. The values of the 10 constants must be determined for a given soil if the model is to be used in numerical simulations of single element laboratory tests or geotechnical boundary value problems where both saturated and unsaturated conditions occur. In addition, the initial state of the soil must be specified for any numerical simulation, including appropriate variation of this initial state with position (e.g. with depth) in a boundary value problem.

Soil constants

The values of soil constants λ , κ and N can be determined from conventional isotropic loading and unloading stages performed in a triaxial apparatus on saturated samples. The value of M can be determined from experimental critical state data for saturated

and unsaturated samples plotted in the $q : p^*$ plane (see Equation 16), and the value of G can be measured in triaxial shear tests on saturated or unsaturated samples (ideally involving unload-reload stages).

It might appear that the values of soil constants λ_s and R would best be determined from conventional water retention curves (measured, for example in a pressure plate test) plotted in the $S_r : \ln s^*$ plane, with λ_s given by the gradient of the main drying and main wetting curves and R calculated from the spacing of the main drying curve and the main wetting curve. However, this procedure would often give misleading values for λ_s and R, because conventional water retention tests will often involve plastic volumetric strains, and under these conditions the GCM predicts that the gradients and spacing of the main drying and main wetting curves do not correspond simply to λ_s and R. A better alternative is therefore to use experimental data from isotropic loading under unsaturated conditions (at a minimum of two different values of suction) to define the unsaturated isotropic normal compression planar surfaces for v and S_r corresponding to the intersection of *M* and *WR* yield surfaces, and to use the gradients and intercepts of these surfaces to determine the values of the soil constants k_1, k_2, λ_s and N^*.

When plotted in $v : \ln p^* : \ln s^*$ space, the intercept of the experimental unsaturated normal compression surface for v gives the value of the soil constant N^* directly (Equation 23). With values of λ and κ already determined from tests on saturated samples, the two gradients λ^* and k_1^* of the experimental unsaturated normal compression surface for v (see Equation 23) can then be used to determine values for the soil constants k_1 and k_2, by combining Equations 21 and 22 to give:

$$k_1 = \frac{k_1^*}{\lambda^* - \kappa} \tag{44}$$

$$k_2 = \frac{\lambda^* - \lambda}{k_1^*} \tag{45}$$

The corresponding experimental unsaturated normal compression surface for S_r (see Equation 24) can then be used to determine the value of the soil constant λ_s. With $\kappa_s = 0$ and values already determined for the soil constants λ, κ, N, N*, k_1 and k_2, Equations 40, 36 and 37 show that the intercept Ω^* and the two gradients, λ_s^* and k_2^*, of the unsaturated normal compression surface for S_r all depend solely on the value of λ_s. Least-squares fitting of Equation 24 to the experimental data defining the planar surface in $S_r : \ln p^* : \ln s^*$ space, with the value of λ_s as the sole degree of freedom, can be used to determine a value for λ_s.

The procedure described above for determining the values of N*, k_1, k_2 and λ_s, allows three degrees of freedom (the values of N*, k_1 and k_2) for fitting the intercept and the two gradients of the unsaturated normal compression surface for v, but only a single degree of freedom (the value of λ_s) for fitting the intercept and the two gradients of the unsaturated normal compression surface for S_r. If this results in poor fitting of the experimental data defining the unsaturated normal compression surface for S_r, it may be appropriate to perform iterative adjustment of parameter values, to improve the fit of the surface for S_r, whilst slightly compromising the fit of the surface for v.

The final soil constant R is required only if the GCM is to be used for simulations involving yielding on both *WR* and *DR* retention yield surfaces. The value of R can be determined by comparing experimental values of v for isotropic stress states at the intersection of *DR* and *M* yield surfaces with Equation 29 (with $\kappa_s = 0$). Suitable experimental tests would include drying of samples starting in normally consolidated saturated states.

The methodology for determining the values of λ, κ, N, N*, k_1, k_2 and λ_s was applied to the experimental results of Sivakumar [41], including saturated and unsaturated tests, resulting in the values shown in Table 3.

Initial state

The initial state of the soil must be specified for any numerical simulation. For the GCM, this initial state is represented by initial values of the stress variables σ_{ij}^* and s^* (p^*, q and s^* are sufficient for the case of a triaxial test) and initial values of the hardening parameters p_0^* and s_1^* (or s_2^*).

For simulations of laboratory tests, it is likely that the initial state will be known in terms of initial values of conventional stress variables, $\bar{p}$, q and s, and initial values of v and S_r. These can be combined to give initial values of p^*, q and s^* (Equations 1 and 3). With the values of soil constants already determined, the general expressions for v and S_r of Equations 27 and 28 can be combined (using $\kappa_s = 0$ and Equations 21, 22, 36 and 37) to give expressions for the initial values of the hardening parameters p_0^* and s_1^* in terms of the initial values of p^*, v and S_r (the initial value of s^* is not involved, because of the assumption $\kappa_s = 0$):

$$\ln p_0^* = \frac{\mathrm{N}^* - v - \kappa \ln p^*}{\lambda - \kappa} + \frac{k_1 \left(\Omega^* - S_r\right)}{\lambda_s} \tag{46}$$

$$\ln s_1^* = \frac{\Omega^* - S_r}{\lambda_s} + \frac{k_2 \left(\mathrm{N}^* - v - \kappa \ln p^*\right)}{\lambda - \kappa} \tag{47}$$

where Ω^* is given by Equation 40.

Having calculated initial values of p_0^* and s_1^* from Equations 46 and 47, these should be checked to ensure that the initial stress state does not fall outside any of the yield surfaces. If this condition is not satisfied, it will be necessary to adjust slightly the initial value of S_r or v (accepting that it will not then perfectly match the experimental value) in order to adjust the values of p_0^* and s_1^* (Equations 46 and 47) such that the initial stress state now falls on or inside the relevant yield surface. Similar adjustment of the initial value of v or S_r may be required if experimental evidence suggests that the initial stress state lies exactly on one of the yield surfaces. To bring the initial stress state exactly on to one of the yield surfaces, through adjustment of the initial value of S_r or v, it will normally be necessary to employ an iterative procedure, because the

initial stress state is normally known in terms of the conventional stress parameters $\bar{p}$, q and s (rather than p^*, q and s^*), and adjustment of the initial value of S_r or v will then lead to a change of the initial value of p^* or s^* (see Equations 1 and 3).

The methodology for determining initial state described above was applied to the tests of Sivakumar [41], for the initial state corresponding to the start of the isotropic loading stage of those tests performed at a suction of 300 kPa ($\bar{p} = 50$ kPa, $q = 0$, $s = 300$ kPa). The corresponding average initial experimental values of v and S_r measured for this group of tests were 2.210 and 0.597 respectively. Experimental evidence suggested that the initial state was on the *WR* yield surface but not necessarily on the *M* yield surface (plastic increase of S_r but no plastic volumetric strain (no collapse compression) occurred during the preceding wetting from the much higher as-compacted value of suction). The procedure to calculate the initial values of p^* and s^* and the initial values of the hardening parameters p_0^* and s_1^* (using Equations 46 and 47) therefore included iterative adjustment of the initial value of S_r to ensure that the initial state fell exactly on the *WR* yield surface ($s^* = s_1^*$). The values of soil constants used in this process were those previously determined and shown in Table 3. The resulting initial value of S_r was 0.562 (rather than the average experimental value of 0.597) and the full calculated initial state conditions are given in Table 4.

For simulations of boundary value problems, the initial state will typically vary with depth within a given soil layer. To represent this, the variations with depth of initial stress state and stress history in terms of net stresses $\bar{\sigma}_{ij}$ and suction s will first need to be estimated, using similar procedures to those employed for boundary value problems involving saturated conditions. This information will then need to be combined with the relevant GCM model equations, and the values of the 10 GCM constants for the particular soil (typically determined from laboratory test data), to estimate the variation with depth of the initial stress state in terms of Bishop's stresses σ_{ij}^* and modified suction s^* and the variation with depth of the initial values of the hardening parameters p_0^* and s_1^*.

Once the initial state of a boundary value problem has been specified, it is useful to express the incremental mechanical and water retention relationships of the GCM, in terms of the increments of strains $\Delta\boldsymbol{\varepsilon}$ and the increments of matric suction Δs (see [23, 24]) because, together, they define an initial value problem that can be integrated over time at each *Gauss* or *integration* point within each finite element (i.e. *local* level). This is the common procedure used in the literature for finite element analysis involving unsaturated soils [5, 38, 43], because these two increments (i.e. $\Delta\boldsymbol{\varepsilon}$, Δs) can be easily approximated at the corresponding integration points, once the nodal displacements and pore fluid pressures increments have been found from the discretized *global* equations.

SIMULATIONS OF EXPERIMENTAL DATA OF SIVAKUMAR (1993)

Validation of the GCM was undertaken by performing model simulations of the experimental tests of Sivakumar [41] performed on saturated and unsaturated samples of compacted speswhite kaolin at suctions of 0, 100, 200 and 300 kPa. Model simulations of initial equalisation stages and isotropic loading stages are discussed here, whereas model simulations of subsequent shearing stages are discussed elsewhere ([24, 26]). Model simulations were performed using the set of values for soil constants shown in Table 3.

All simulations commenced from the same initial state A, corresponding to the end of the initial equalisation stage for those samples tested at a suction of 300 kPa, as shown in Table 4. For tests conducted at suctions of 200kPa or 100kPa the simulations commenced with an initial wetting stage, AB or AC respectively, (at $\bar{p}$ = 50 kPa) from $s = 300\,\text{kPa}$ to the required value of *s*, to represent the remainder of the initial equalisation stage for these tests. For tests conducted at zero suction the simulations were designed to replicate the stress path followed by Sivakumar [41] in the initial equalisation stage of his tests on saturated samples. This required initial isotropic unloading AD (at $s = 300\,\text{kPa}$) from $\bar{p} = 50\,\text{kPa}$ to $\bar{p} = 40\,\text{kPa}$, followed by wetting DE (at $\bar{p} = 40\,\text{kPa}$) from $s = 300\,\text{kPa}$ to $s = 0$, and then finally isotropic unloading EF (at $s = 0$) from $\bar{p} = 40\,\text{kPa}$ to $\bar{p} = 25\,\text{kPa}$. These procedures ensured that simulations performed at all four values of suction employed consistent initial states at

the start of the subsequent isotropic loading stages, with differences of v and S_r that were consistent with model predictions.

Figures 19 and 20 show experimental variations of v against p^* and $\bar{p}$ respectively (with stresses on both linear and logarithmic scales) from the isotropic loading stages performed at all four different values of suction, plotted together with the corresponding model simulations. Variations of S_r are presented in Figure 21 against p^*. In Figures 19-21, model simulations of the initial equalisation stages from the common starting point A are indicated by dashed lines, simulations of constant suction isotropic loading stages are indicated by thick solid lines and experimental results for isotropic loading stages are indicated by symbols joined by thinner solid lines.

Inspection of Figures 19 and 21 shows that the GCM simulations capture the observed changes of v and S_r during the equalisation stages of the tests conducted at suctions of 200kPa, 100kPa and 0, relative to the common starting point A of the simulations. As a consequence, the predicted values of v and S_r at the start of the isotropic loading stages of these tests (points B, C and F) show reasonable agreement with the corresponding experimental values (predicted values of v at C and F are slightly too high and slightly too low, respectively).

In particular, the model simulations correctly predict, at a qualitative level, the complex pattern of swelling and collapse compression reported by Sivakumar [41] during wetting DE to zero suction in the tests conducted on saturated samples. During the first part of this wetting, from D to Y (see Figure 19), the soil state is on the *WR* yield surface but inside the *M* yield surface, and elastic swelling is predicted (due to the decrease of p^*). Coupled inward movements of the *M* yield surface occur, such that yield on the *M* surface commences at Y, and then collapse compression is predicted from Y to S, where the soil reaches a saturated state (at a non-zero air-exclusion value of suction). From S to E, with the soil in a saturated condition, the model prediction shows elastic swelling, due to the reduction of p^* (where $p^* = p'$ in this saturated condition), as suction is reduced from the air-exclusion value to a final value of zero. Sivakumar [41] observed the same qualitative pattern of behaviour in his experimental tests, with initial wetting-induced swelling followed by wetting-induced collapse compression and then finally more wetting-induced swelling. Conventional models expressed in terms of net

stresses and suction (such as the BBM) would be unable to predict the final phase of wetting-induced swelling.

Inspection of Figure 19 shows that the GCM simulations provide an excellent match to the experimental positions of the normal compression lines at the four different values of suction in the $v:\ln p^*$ plane. This is a consequence of selecting the values of the model parameters λ, N, N^*, k_1 and k_2 to fit the saturated isotropic NCL and the unsaturated isotropic normal compression planar surface in $v:\ln p^*:\ln s^*$ space. The fact that the GCM simulations for v at the four different values of suction also match well the experimental normal compression lines when plotted in the $v:\ln \bar{p}$ plane (see Figure 20) indicates that the model has also been able to provide adequate modelling of the variation of S_r, given that conversion of experimental and predicted values of p^* to corresponding values of $\bar{p}$ involves the experimental and predicted values of S_r (see Equation 1).

Figure 21 shows that the GCM predictions for the variations of S_r at the three non-zero values of suction provide a reasonable match to the experimental results, but the match is not as good as for the corresponding variations of v (see Figure 19). This is a consequence of allowing 3 degrees of freedom (the values of N^*, k_1 and k_2) when fitting the experimental data defining the unsaturated normal compression surface for v, but only 1 degree of freedom (the value of λ_s) when fitting the data defining the normal compression surface for S_r. It would have been possible to improve the fit of the predicted variations of S_r, by adjusting some of the model parameter values, but this would have been at the expense of slight deterioration in the fit of the predicted values of v.

A significant conclusion arises from comparison of Figure 19b and Figure 20b: whereas a clear pattern emerges from the experimental normal compression lines for different values of suction when plotted in the $v:\ln p^*$ plane, no such pattern is apparent when the same experimental curves are plotted in the $v:\ln \bar{p}$ plane. In the $v:\ln p^*$ plane (Figure 19b), the constant suction experimental normal compression lines corresponding to unsaturated conditions (at suctions of 100kPa, 200kPa and 300kPa) approximate to straight parallel lines, whereas the saturated normal compression line

forms a straight line of lower gradient. This pattern is perfectly represented by the GCM, which predicts that constant s isotropic normal compression lines corresponding to unsaturated conditions approximate to straight parallel lines of gradient λ^* in the $v:\ln p^*$ plane (the GCM would predict perfectly straight parallel lines of gradient λ^* if s^* were held constant (see Equation 23), rather than s), whereas the GCM predicts a saturated isotropic normal compression line of lower gradient λ. In contrast, when the same experimental curves are re-plotted in the $v:\ln \bar{p}$ plane (Figure 20b), the variation of normal compression line gradient with suction appears complex and without clear pattern. Despite this, the GCM manages to predict well the complex form of the various normal compression lines in the $v:\ln \bar{p}$ plane, because the GCM is developed in the $v:\ln p^*$ plane, where the experimental results show a logical pattern, and only then transferred to the $v:\ln \bar{p}$ plane. This provides a strong argument in favour of developing models that employ mean Bishop's stress p^* as a stress state variable, rather than mean net stress $\bar{p}$.

Various previous authors have proposed mechanical constitutive models that involve relatively complex relationships attempting to represent variations of a virgin compression index λ with suction (Alonso et al. [1]; Wong and Mašín [52]), with degree of saturation (Zhou and Sheng [53]) or with both s and S_r (Alonso et al. [3]). The evidence presented in Figure 19b suggests that such complexity may be overcome by developing models that use p^* as stress state variable and fully account for the coupling between mechanical and water retention behaviour.

CONCLUSIONS

The Glasgow Coupled Model (GCM) predicts that isotropic normal compression states and critical states in experimental tests involving plastic volumetric strains and plastic increases of S_r will correspond to points at the intersection of *M* and *WR* yield surfaces. For these states, the model predicts unique unsaturated isotropic normal compression and unsaturated critical state planar surfaces for specific volume v (in $v:\ln p^*:\ln s^*$ space) and also unique isotropic normal compression and critical state planar surfaces

for degree of saturation S_r (in S_r: $\ln p^* : \ln s^*$ space). Experimental results from the tests of Sivakumar [41] on unsaturated samples of compacted speswhite kaolin provide confirmation of the existence and form of these unique unsaturated normal compression and critical state surfaces. The GCM also provides expressions for the values of v and S_r for any general stress states, in terms of the values of the stresses p^* and s^* and the values of the hardening parameters p_0^* and s_1^*.

The GCM provides consistent representation of transitions between saturated and unsaturated states, including the influence of retention hysteresis and the effect of plastic volumetric strains on retention behaviour. The GCM gives unique expressions to predict saturation and de-saturation conditions (air-exclusion and air-entry points respectively), in the form of two unique straight lines in the $\ln s^* : \ln p_0^*$ plane. The saturated normal compression line (NCL) plots as a planar surface in both $v : \ln p^* : \ln s^*$ and $S_r : \ln p^* : \ln s^*$ spaces, and when transitions from unsaturated to saturated conditions occur under isotropic stress states at the intersection of *M* and *WR* yield surfaces, the saturation line corresponds to the intersection of unsaturated and saturated isotropic normal compression planar surfaces in both spaces.

The GCM provides consistent modelling of mechanical behaviour across the transitions between saturated and unsaturated conditions, including appropriate representation of the variation of mechanical yield stress. This appropriate variation of mechanical yield stress across transitions between unsaturated and saturated conditions occurring at non-zero values of suction emerges naturally from the GCM, whereas it would be very difficult to achieve in any mechanical model expressed in terms of net stresses and suction.

A straightforward methodology is proposed (and has been demonstrated) for determining the values of all GCM model parameters and initial state from a limited number of suction-controlled triaxial tests. Central to this methodology is plotting the experimental data defining the unsaturated isotropic normal compression planar surfaces in $v : \ln p^* : \ln s^*$ and $S_r : \ln p^* : \ln s^*$ spaces.

GCM simulations of the isotropic loading stages of the experimental tests of Sivakumar [41] on compacted speswhite kaolin demonstrate that the model is able to predict accurately the variations of both v and S_r during isotropic stress paths under saturated and unsaturated conditions. A clear pattern emerges when the experimental results for unsaturated and saturated isotropic normal compression states are plotted against $\ln p^*$, whereas no such pattern is apparent when the same results are plotted against $\ln \bar{p}$. The GCM represents the clear pattern observed in the $v : \ln p^*$ plane and, as a consequence, also captures the complex variation of the experimental results when re-plotted in the $v : \ln \bar{p}$ plane. This would be extremely difficult to achieve with any constitutive model developed in terms of net stresses and suction, and this provides a strong argument in favour of models, such as the GCM, which employ p^* as a stress state variable.

ACKNOWLEDGEMENTS

The first author acknowledges the financial support by the *Synergy* Postgraduate Scholarships scheme and the Australian Research Council Centre of Excellence in Geotechnical Science and Engineering (CGSE).

REFERENCES

1. Alonso EE, Gens A, Josa A (1990) A constitutive model for partially saturated soils. Géotechnique 40(3):405–430
2. Alonso EE, Olivella S, Pinyol NM (2005) A review of Beliche Dam. Géotechnique 55(4):267–285
3. Alonso EE, Pinyol NM, Gens A (2013) Compacted soil behaviour: initial state, structure and constitutive modelling. Géotechnique 63(6):463–478
4. Bishop AW (1959) The principle of effective stress. Tek. Ukeblad 39, 859–863
5. Borja RI (2004) Cam-Clay plasticity, Part V: A mathematical framework for three-phase deformation and strain localization analyses of partially saturated porous media. Comput Methods Appl Mech Eng 193: 5301–5338
6. Borja RI, White JA (2010) Continuum deformation and stability analyses of a steep hillside slope under rainfall infiltration. Acta Geotech 5:1–14

7. Borja RI, Liu X, White JA (2012) Multiphysics hillslope processes triggering landslides. Acta Geotech 7:261–269

8. Burton GJ, Sheng D, Airey D (2014) Experimental study on volumetric behaviour of Maryland clay and the role of degree of saturation. Can Geotech J 51:1449–1455

9. Buscarnera G, Nova R (2009) An elasto-plastic strain hardening model for soil allowing for hydraulic bonding debonding effects. Int J Numer Anal Meth Geomech 33:1055–1086

10. Casini F (2008) Effetti del grado di saturazione sul comportamento meccanico di un limo. PhD Thesis, Universitá degli Studi di Roma ‘‘La Sapienza’’

11. Casini F, Serri V, Springman SM (2013) Hydromechanical behaviour of a silty sand from a steep slope triggered by artificial rainfall: from unsaturated to saturated conditions. Can Geotech J 50:28–40

12. Della Vecchia G, Romero E, Jommi C (2013) A fully coupled elastic–plastic hydromechanical model for compacted soils accounting for clay activity. Int J Numer Anal Meth Geomech 37:503–535

13. D'Onza F, Gallipoli D, Wheeler SJ, Casini F, Vaunat J, Khalili N, Laloui L, Mancuso C, Mašín D, et al. (2011) Benchmark of constitutive models for unsaturated soils. Géotechnique 61(4): 283–302

14. D'Onza F, Wheeler SJ, Gallipoli D, Barrera M, Hofmann M, Lloret-Cabot M, Lloret A, Mancuso C, Pereira J-M et al. (2015) Benchmarking selection of parameter values for the Barcelona basic model. Engineering Geology 196:99–118

15. Gallipoli D, Wheeler SJ, Karstunen M (2003) Modelling the variation of degree of saturation in a deformable unsaturated soil. Géotechnique 53(1):105–112

16. Gallipoli D, Gens A, Chen G, D'Onza F (2008) Modelling unsaturated soil behaviour during normal consolidation and at critical state. Comp Geotech 35(6):825–834

17. Gens A (2010) Soil–environment interactions in geotechnical engineering. Géotechnique 60(1):3–74

18. Houlsby GT (1997) The work input to an unsaturated granular material. Géotechnique 47(1):193–196

19. Jommi C (2000) Remarks on the constitutive modelling of unsaturated soils. In: Tarantino A, Mancuso C (ed) Experimental evidence and theoretical approaches in unsaturated soils. Rotterdam: Balkema, pp 139-153

20. Josa A (1988) Un modelo elastoplastico para suelos no saturados. PhD Thesis, Universitat Politècnica de Catalunya

21. Khalili N, Habte MA, Zargarbashi S (2008) A fully coupled flow deformation model for cyclic analysis of unsaturated soils including hydraulic and mechanical hysteresis. Comp Geotech 35(6):872–889

22. Laloui L, Ferrari A, Li C, Eichenberger J (2016) Hydro-mechanical analysis of volcanic ash slopes during rainfall. Géotechnique 66(3):220–231

23. Lloret M. (2011) Numerical modelling of coupled behaviour in unsaturated soils. PhD Thesis, University of Strathclyde and University of Glasgow

24. Lloret-Cabot M, Sánchez M, Wheeler SJ (2013) Formulation of a three-dimensional constitutive model for unsaturated soils incorporating mechanical-water retention couplings. Int J Numer Anal Methods Geomech 37:3008–3035

25. Lloret-Cabot M, Wheeler SJ, Sánchez M (2014) Unification of plastic compression in a coupled mechanical and water retention model for unsaturated soils. Can Geotech J 51(12):1488–1493

26. Lloret-Cabot M, Wheeler SJ, Pineda JA, Sheng D, Gens A (2014). Relative performance of two unsaturated soil models using different constitutive variables. Can Geotech J 51(12):1423–1437

27. Mašín D (2010) Predicting the dependency of a degree of saturation on void ratio and suction using effective stress principle for unsaturated soils. Int J Numer Anal Methods Geomech 34:73–90

28. Monroy R (2006) The influence of load and suction changes on the volumetric behaviour of compacted London Clay. PhD Thesis, Imperial College

29. Monroy R, Zdravkovic L, Ridley A (2008) Volumetric behaviour of compacted London Clay during wetting and loading. In: Toll DG, Augarde CE, Gallipoli D, Wheeler SJ (ed) Proc. 1st Eur. Conf. Unsaturated Soils, Durham, pp 315–320

30. Monroy R, Zdravkovic L, Ridley A (2010) Evolution of microstructure in compacted London Clay during wetting and loading. Géotechnique 60(2):105–119

31. Nuth M, Laloui L (2008) Advances in modelling hysteretic water retention curve in deformable soils. Comp Geotech 35(6):835–844

32. Raveendiraraj A (2009) Coupling of mechanical behaviour and water retention behaviour in unsaturated soils. PhD Thesis, University of Glasgow

33. Romero E (1999) Characterisation and thermo-hydro-mechanical behaviour of unsaturated Boom clay: an experimental study. PhD Thesis, Universitat Politècnica de Catalunya

34. Romero E, Della Vecchia G, Jommi C (2011) An insight into the water retention properties of compacted clayey soils. Géotechnique 61(4):313–328

35. Roscoe KH, Burland JB (1968) On the generalised stress-strain behavior of 'wet' clay. In: Heyman J Leckie FA (ed) Engineering Plasticity, Cambridge University Press, pp 535–609

36. Schrefler BA (1984) The finite element method in soil consolidation (with applications to surface subsidence). PhD Thesis, University College of Swansea

37. Sharma RS (1998) Mechanical behaviour of unsaturated highly expansive clays. PhD Thesis, University of Oxford

38. Sheng D (2011) Review of fundamental principles in modelling unsaturated soil behaviour. Comp Geotech 38: 757–776

39. Sheng D, Fredlund DG, Gens A (2008) A new modelling approach for unsaturated soils using independent stress variables. Can Geotech J 45:511–534

40. Sheng D, Zhou A (2011) Coupling hydraulic with mechanical models for unsaturated Soils. Can Geotech J 48:826–840

41. Sivakumar V (1993) A critical state framework for unsaturated soil. PhD Thesis, University of Sheffield

42. Sivakumar V, Wheeler SJ (2000) Influence of compaction procedure on the mechanical behaviour of an unsaturated compacted clay, Part 1: Wetting and isotropic compression. Géotechnique 50(4):359–368

43. Song X, Borja RI (2014) Mathematical framework for unsaturated flow in the finite deformation range. Int J Numer Meth Eng 14:658–682

44. Sun DA, Sheng D, Xu Y (2007) Collapse behaviour of unsaturated compacted soil with different initial densities. Can Geotech J. 44:673–686

45. Tarantino A, De Col E (2008) Compaction behaviour of clay. Géotechnique 58(3):199–213

46. Tarantino A (2009) A water retention model for deformable soils. Géotechnique 59(9):751–762

47. Tarantino A, Tombolato S (2005) Coupling of hydraulic and mechanical behaviour in unsaturated compacted clay. Géotechnique 55(4):307–317

48. Vaunat J, Romero E, Jommi C (2000) An elastoplastic hydro-mechanical model for unsaturated soils. In: Tarantino A, Mancuso C (ed) Experimental evidence and theoretical approaches in unsaturated soils. Rotterdam: Balkema, pp 121–138

49. Wheeler SJ, Sivakumar V (1995) An elasto-plastic critical state framework for unsaturated soil. Géotechnique 45(1):35–53

50. Wheeler SJ, Näätänen A, Karstunen M, Lojander M (2003) An anisotropic elastoplastic model for soft clays. Can Geotech J 40:403–418

51. Wheeler SJ, Sharma RS, Buisson MSR (2003) Coupling of hydraulic hysteresis and stress–strain behaviour in unsaturated soils. Géotechnique 53(1):41–54

52. Wong KS, Mašín D (2014) Coupled hydro-mechanical model for partially saturated soils predicting small strain stiffness. Comp Geotech 61:355–369

53. Zhou A, Sheng D (2015) An advanced hydro-mechanical constitutive model for unsaturated soils with different initial densities. Comp Geotech 63:46–66

Table 1. Gradients and intercepts of best-fit isotropic normal compression planar surfaces for v and S_r

$\lambda^* = 0.249$	$k_1^* = 0.171$	$\mathrm{N}^* = 2.728$
$\lambda_s^* = 0.204$	$k_2^* = 0.152$	$\Omega^* = 0.780$

Table 2. Gradients and intercepts of best-fit critical state planar surfaces for v and S_r

$\lambda^* = 0.268$	$k_1^* = 0.174$	$\Gamma^* = 2.731$
$\lambda_s^* = 0.236$	$k_2^* = 0.205$	$\Psi^* = 0.733$

Table 3. Values of soil constants for model simulations

$\lambda = 0.123$	$\kappa = 0.010$	N = 2.621	
$\mathrm{N}^* = 2.728$	$k_1 = 0.715$	$k_2 = 0.737$	$\lambda_s = 0.129$

Table 4. Initial state for model simulations

$\bar{p} = 50\,\mathrm{kPa}$	$v = 2.210$	$p^* = 218.5\,\mathrm{kPa}$	$p_0^* = 267.9\,\mathrm{kPa}$
$s = 300\,\mathrm{kPa}$	$S_r = 0.562$	$s^* = 164.3\,\mathrm{kPa}$	$s_1^* = 164.3\,\mathrm{kPa}$

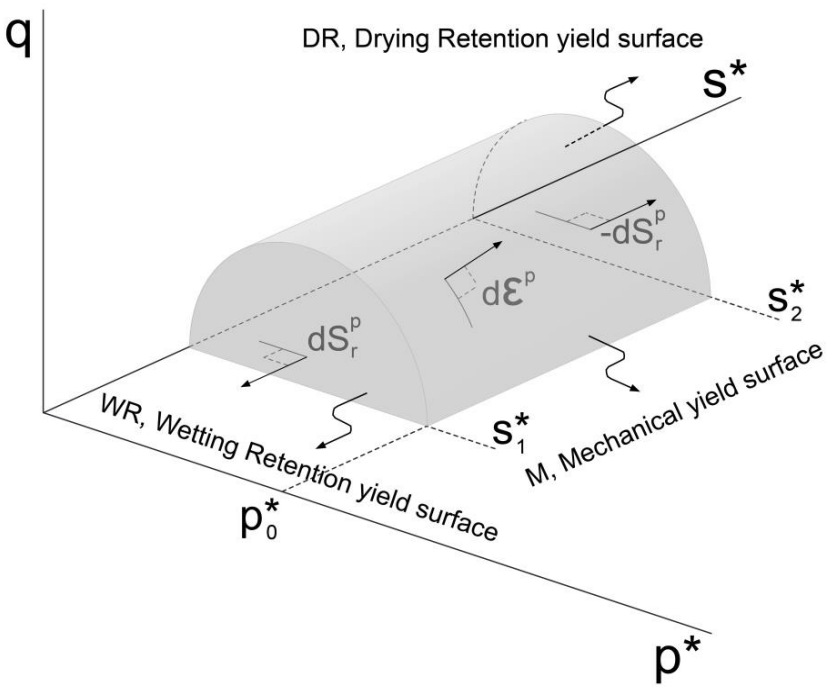

Fig. 1. Yield surfaces in Glasgow Coupled Model (GCM)

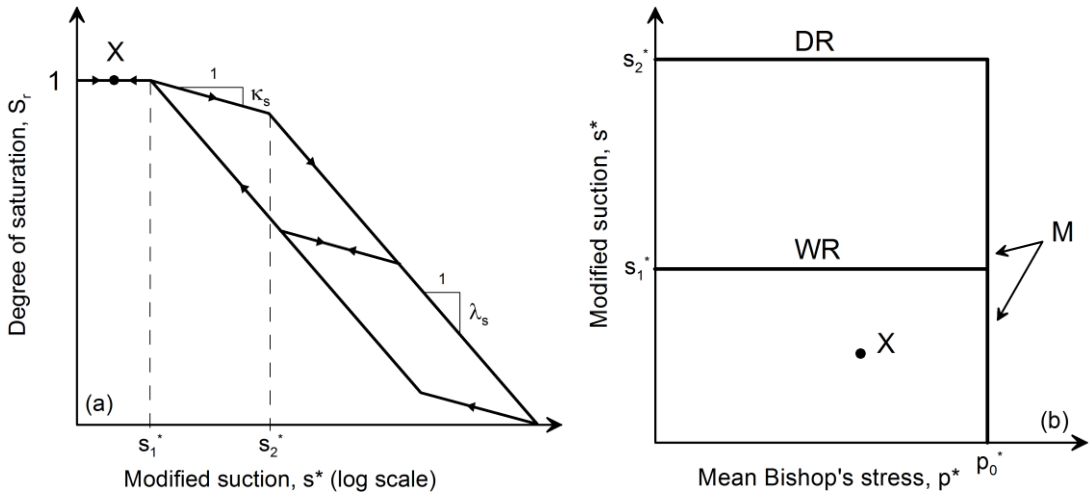

Fig. 2. Modelling retention behaviour and treatment of saturated conditions

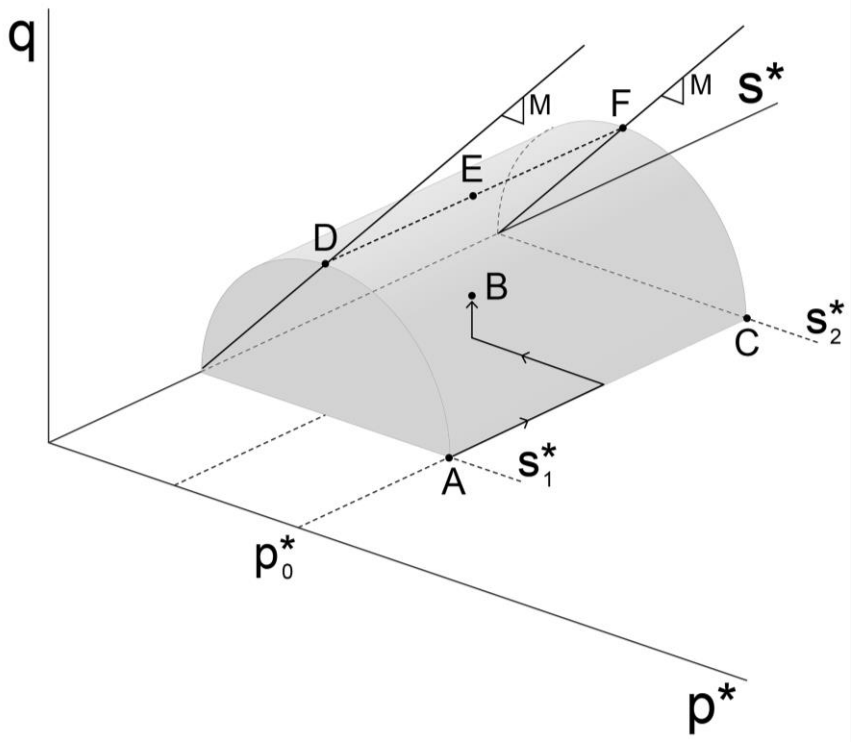

Fig. 3. Positions of various points relative to the yield surfaces

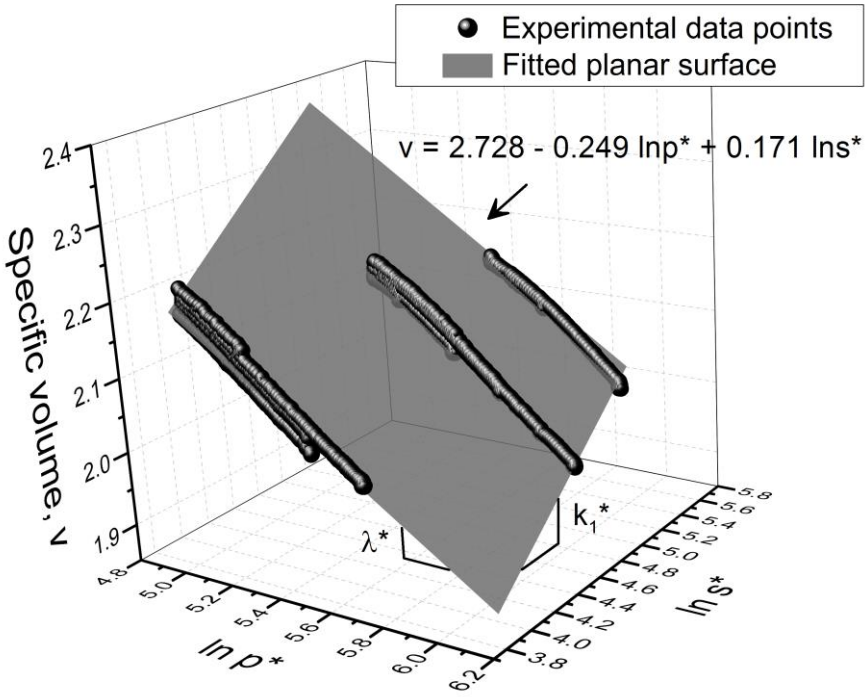

Fig. 4. Isotropic normal compression planar surface for *v* (Sivakumar [41])

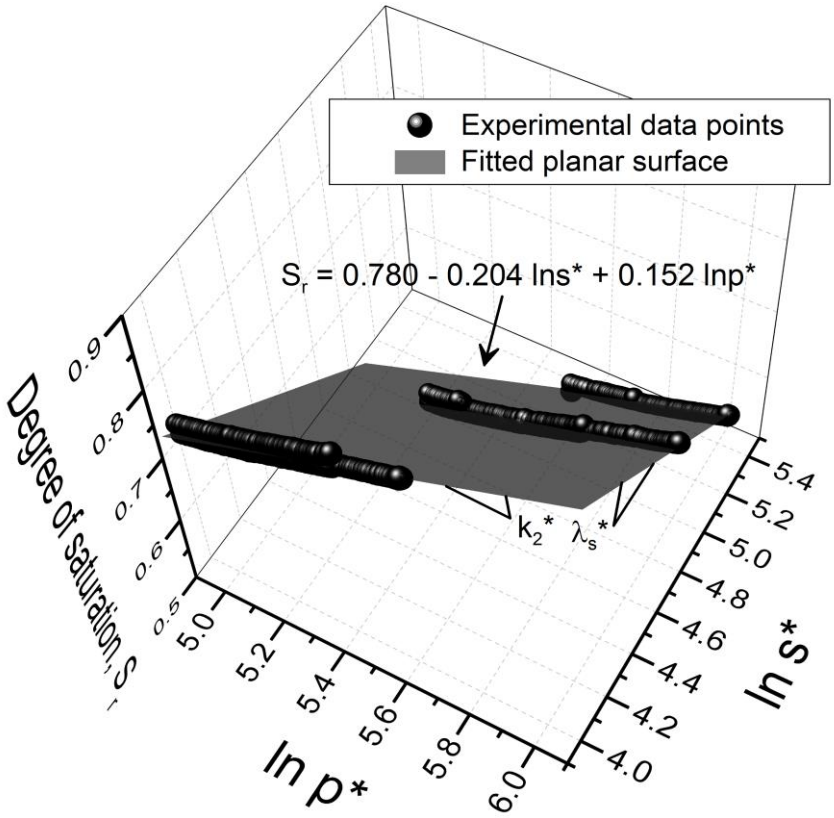

Fig. 5. Isotropic normal compression planar surface for S_r (Sivakumar [41])

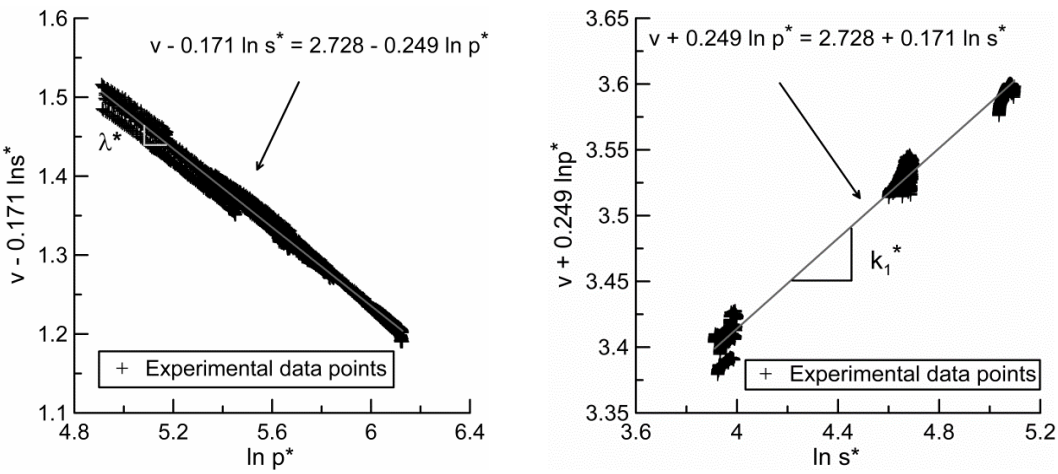

Fig. 6. Orthogonal two-dimensional views of isotropic normal compression planar surface for *v* (Sivakumar [41])

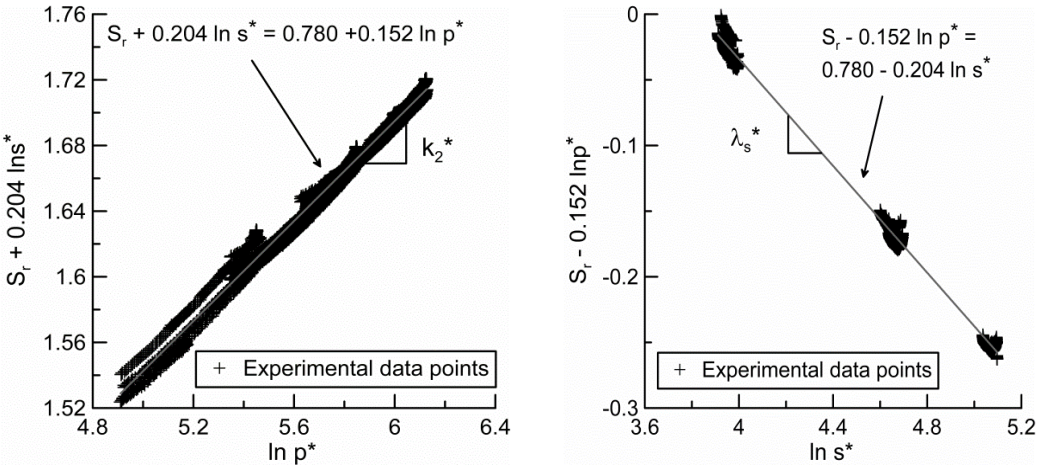

Fig. 7. Orthogonal two-dimensional views of isotropic normal compression planar surface for S_r (Sivakumar [41])

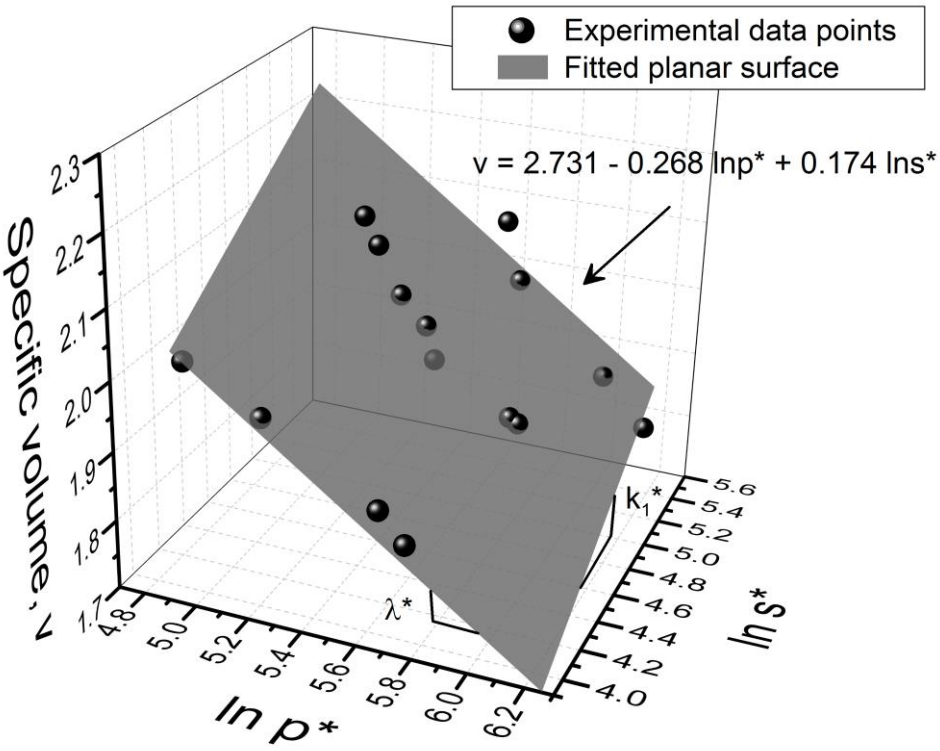

Fig. 8. Critical state planar surface for *v* (Sivakumar [41])

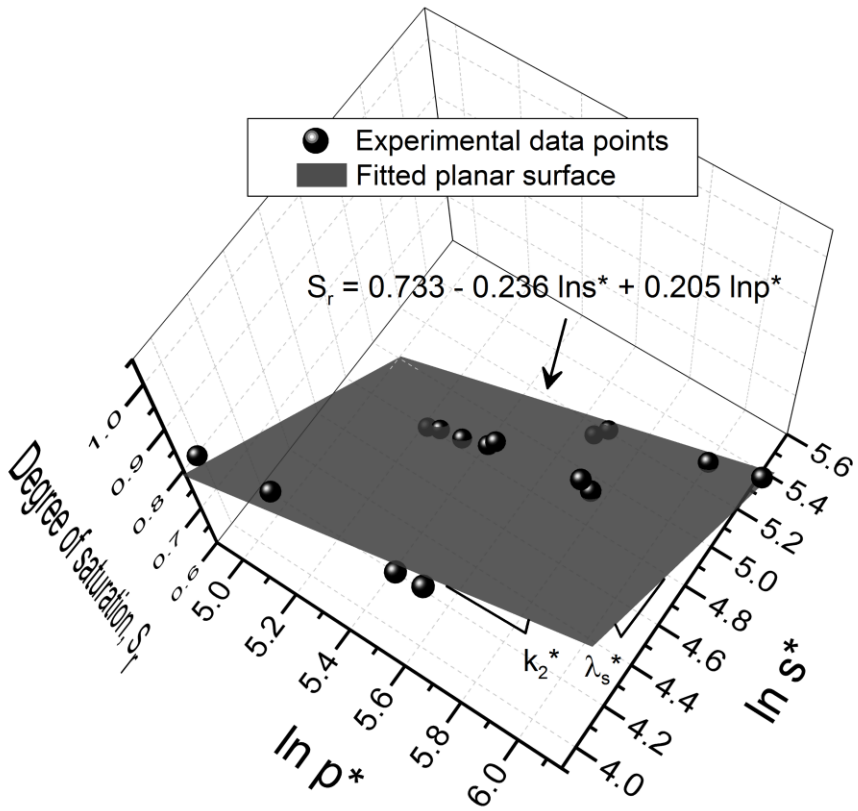

Fig. 9. Critical state planar surface for S_r (Sivakumar [41])

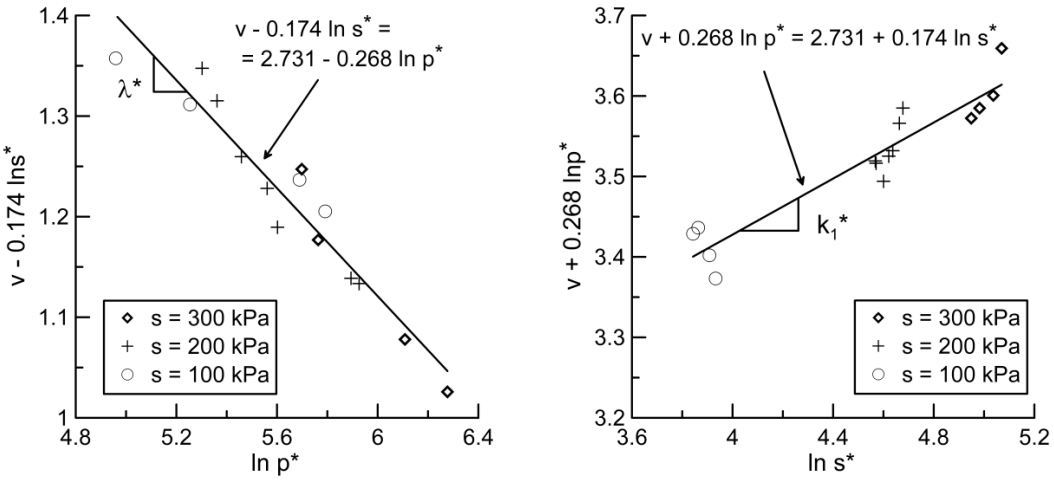

Fig. 10. Orthogonal two-dimensional views of critical state planar surface for v (Sivakumar [41])

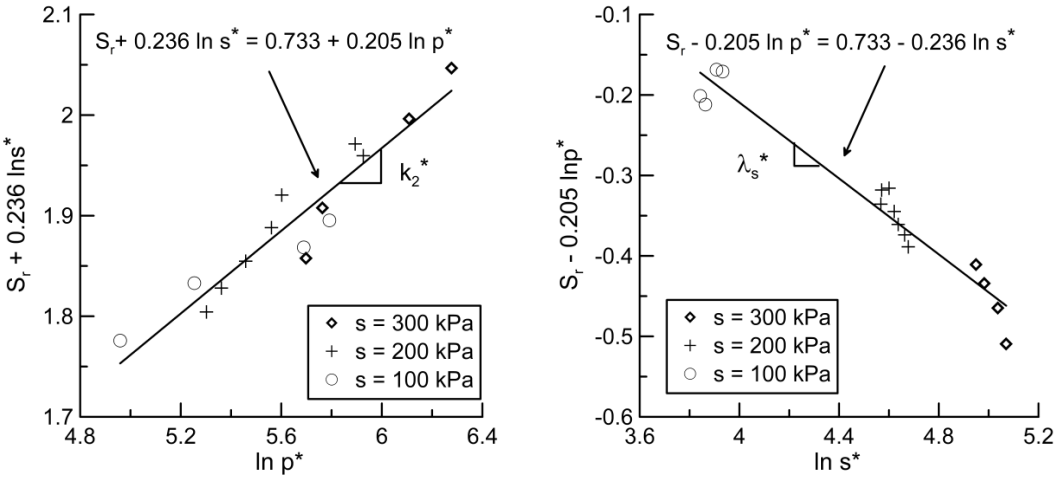

Fig. 11. Orthogonal two-dimensional views of critical state planar surface for S_r (Sivakumar [41])

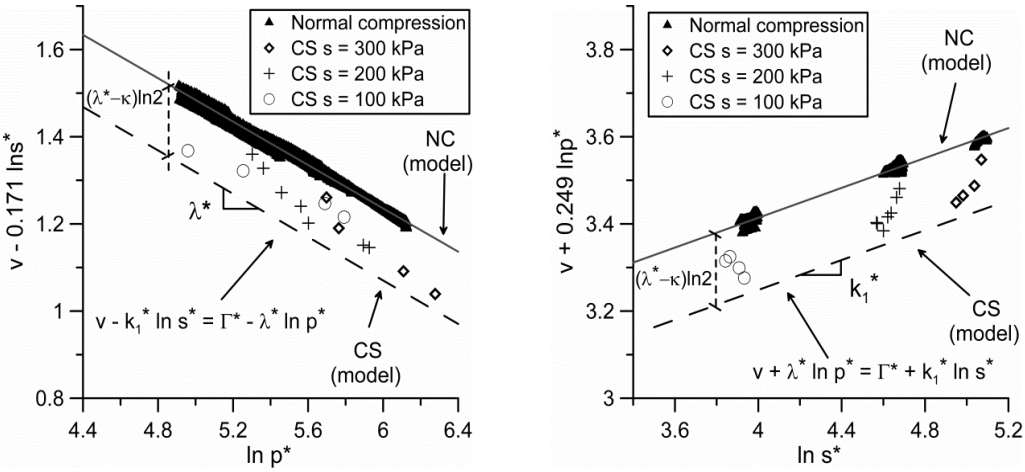

Fig. 12. Orthogonal two-dimensional views of planar surfaces for *v* (Sivakumar [41])

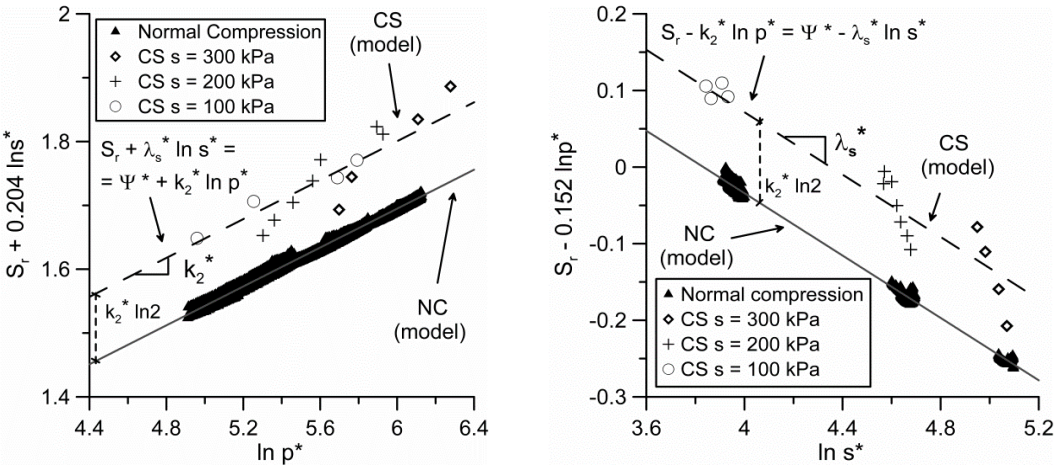

Fig. 13. Orthogonal two-dimensional views of planar surfaces for S_r (Sivakumar [41])

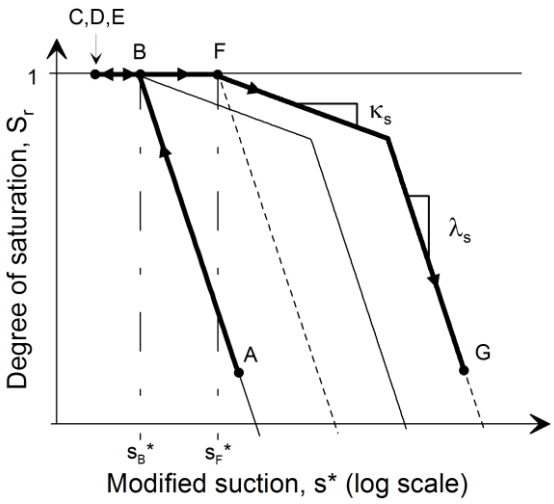

Fig. 14. Demonstration of irreversible elastic changes of S_r if $\kappa_s > 0$

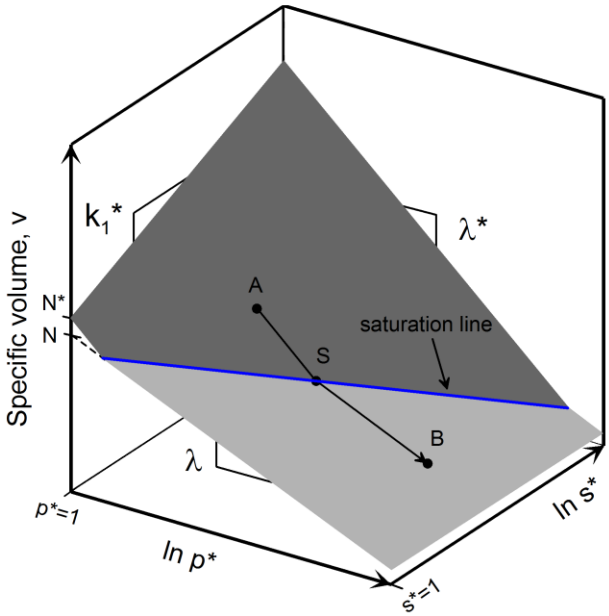

Fig. 15. Isotropic normal compression planar surfaces for *v* for unsaturated and saturated conditions

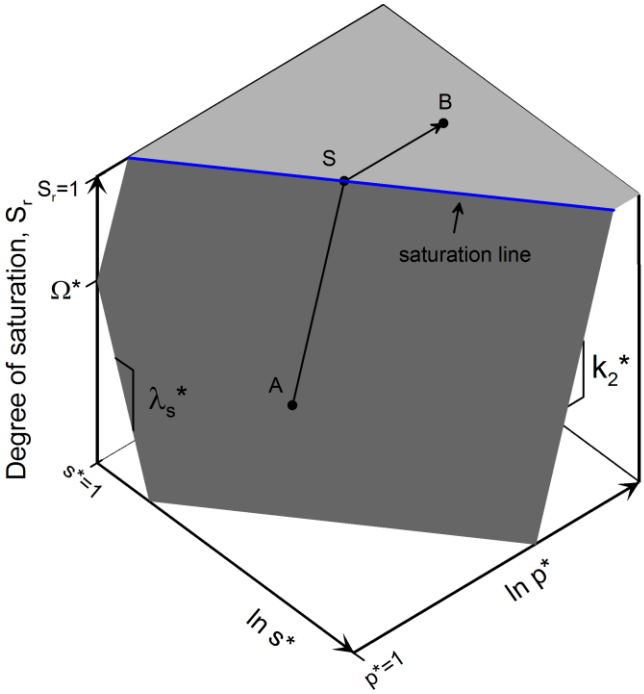

Fig. 16. Isotropic normal compression planar surfaces for S_r for unsaturated and saturated conditions

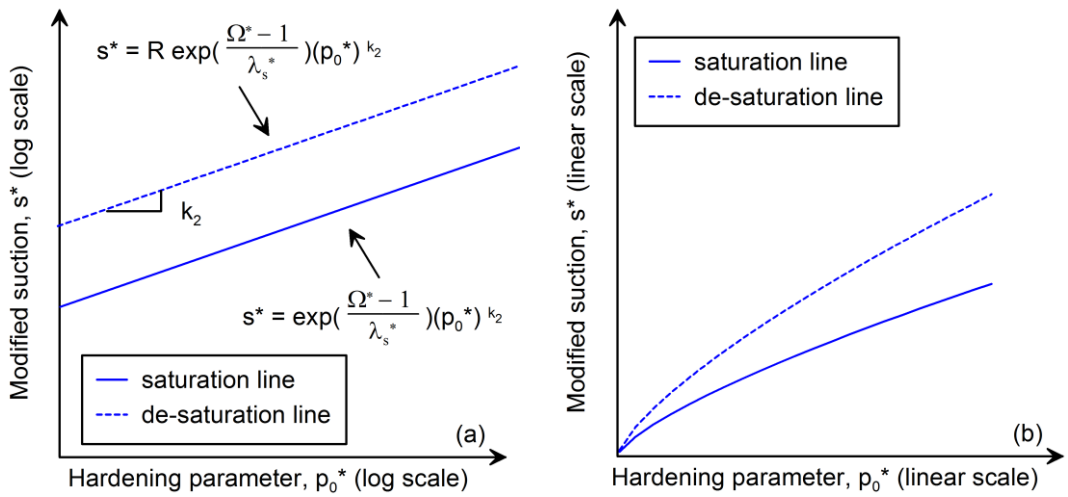

Fig. 17. Predicted saturation and de-saturation lines

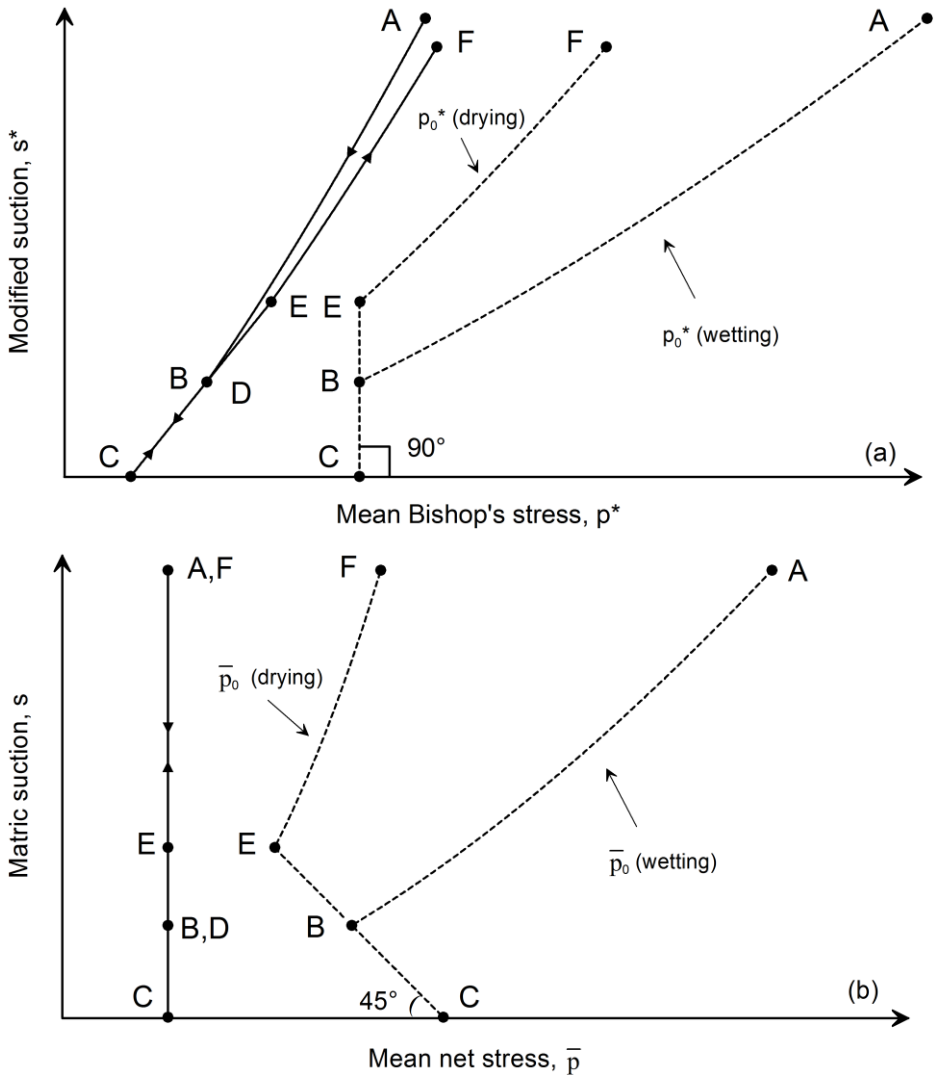

Fig. 18. Variation of mechanical yield stress during a wetting-drying cycle

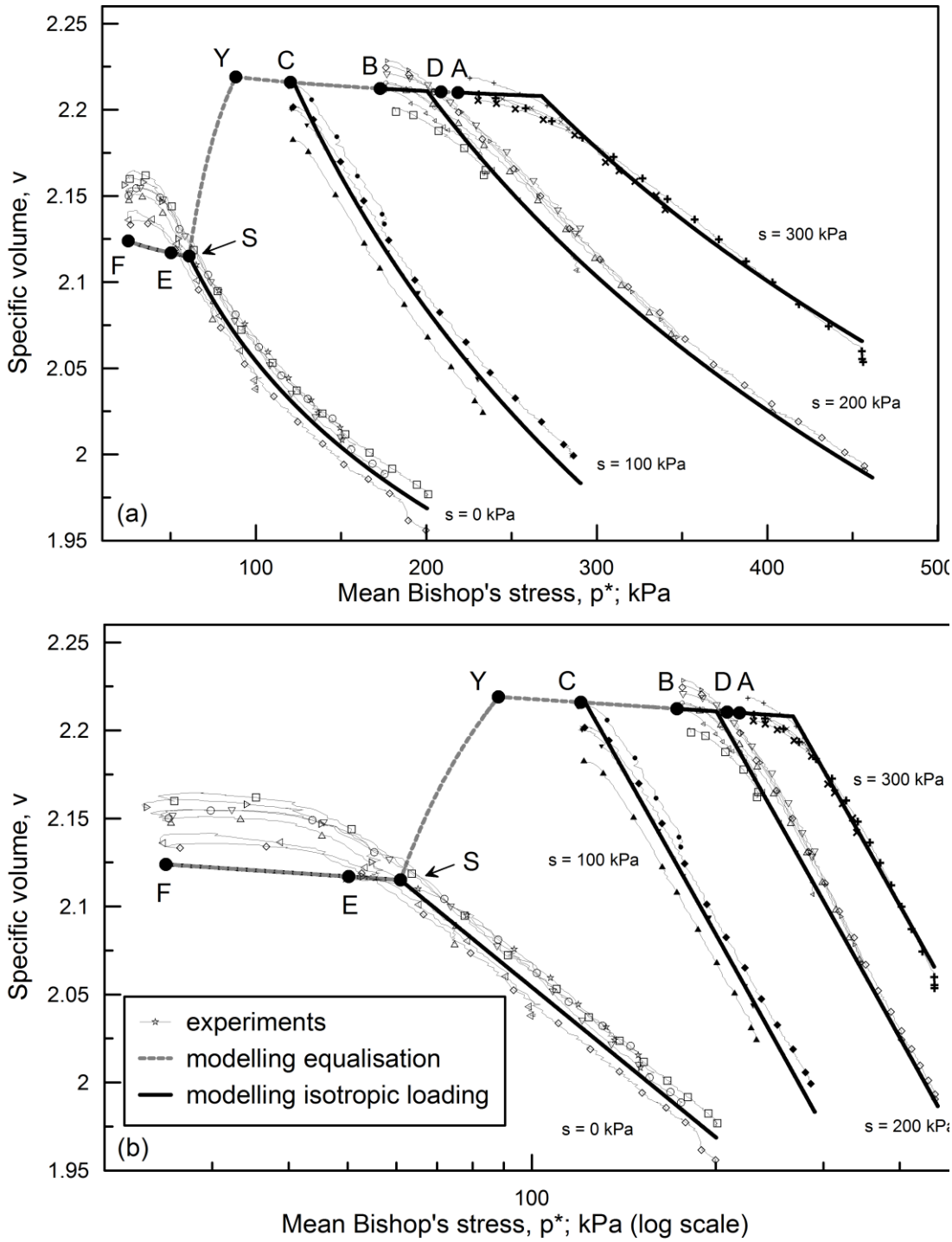

Fig. 19. Model predictions and experimental variations of v against p^* (Sivakumar [41]): (a) Linear scale; (b) Logarithmic scale

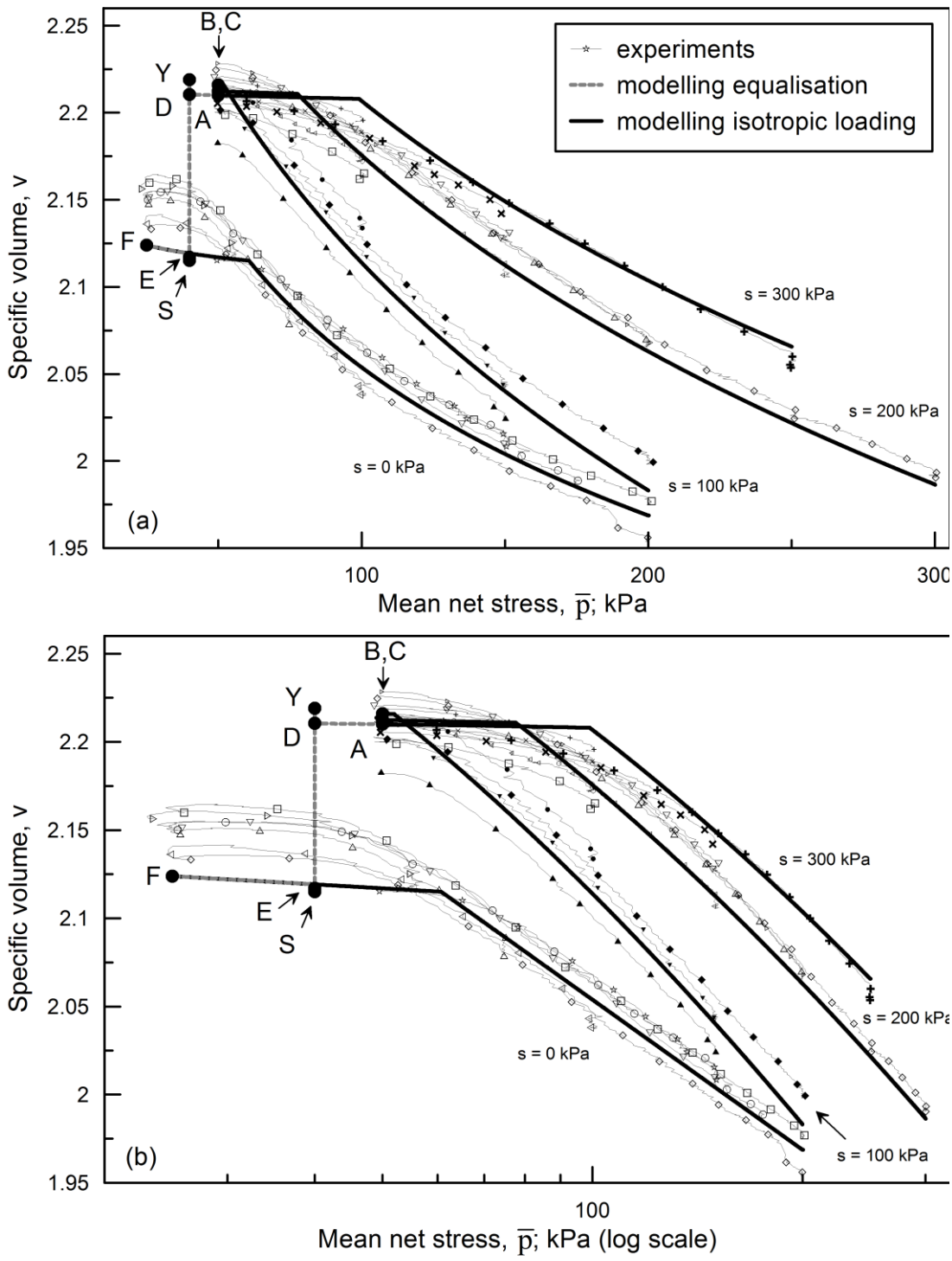

Fig. 20. Model predictions and experimental variations of v against $\bar{p}$ (Sivakumar [41]): (a) Linear scale; (b) Logarithmic scale

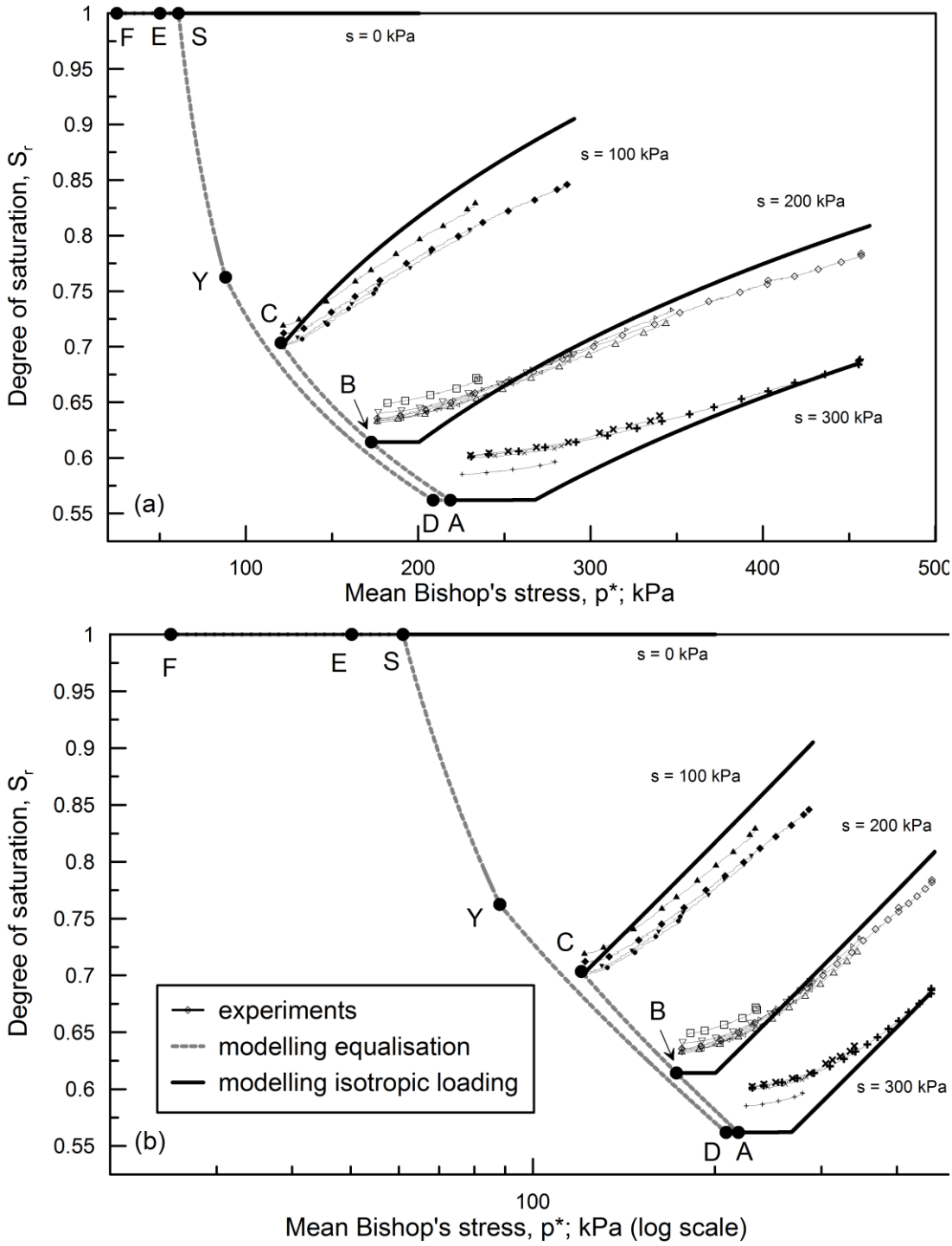

Fig. 21. Model predictions and experimental variations of S_r against p^* (Sivakumar [41]): (a) Linear scale; (b) Logarithmic scale

Fig. 1. Yield surfaces in Glasgow Coupled Model (GCM)

Fig. 2. Modelling retention behaviour and treatment of saturated conditions

Fig. 3. Positions of various points relative to the yield surfaces

Fig. 4. Isotropic normal compression planar surface for v (Sivakumar [41])

Fig. 5. Isotropic normal compression planar surface for S_r (Sivakumar [41])

Fig. 6. Orthogonal two-dimensional views of isotropic normal compression planar surface for v (Sivakumar [41])

Fig. 7. Orthogonal two-dimensional views of isotropic normal compression planar surface for S_r (Sivakumar [41])

Fig. 8. Critical state planar surface for v (Sivakumar [41])

Fig. 9. Critical state planar surface for S_r (Sivakumar [41])

Fig. 10. Orthogonal two-dimensional views of critical state planar surface for v (Sivakumar [41])

Fig. 11. Orthogonal two-dimensional views of critical state planar surface for S_r (Sivakumar [41])

Fig. 12. Orthogonal two-dimensional views of planar surfaces for v (Sivakumar [41])

Fig. 13. Orthogonal two-dimensional views of planar surfaces for S_r (Sivakumar [41])

Fig. 14. Demonstration of irreversible elastic changes of S_r if $\kappa_s > 0$

Fig. 15. Isotropic normal compression planar surfaces for v for unsaturated and saturated conditions

Fig. 16. Isotropic normal compression planar surfaces for S_r for unsaturated and saturated conditions

Fig. 17. Predicted saturation and de-saturation lines

Fig. 18. Variation of mechanical yield stress during a wetting-drying cycle

Fig. 19. Model predictions and experimental variations of v against p^* (Sivakumar [41]): (a) Linear scale; (b) Logarithmic scale

Fig. 20. Model predictions and experimental variations of v against $\bar{p}$ (Sivakumar [41]): (a) Linear scale; (b) Logarithmic scale

Fig. 21. Model predictions and experimental variations of S_r against p^* (Sivakumar [41]): (a) Linear scale; (b) Logarithmic scale